AGU PUBLICATIONS

JGR

Journal of Geophysical Research: Atmospheres

RESEARCH ARTICLE

10.1002/2013JD021255

Key Points:
- Aircraft based, size-resolved, Saharan dust fluxes are measured
- The eddy covariance method is used with particles up to 300 micrometers
- Links to terrain, topography and vertical turbulent kinetic energy are discussed

Supporting Information:
- Readme
- Animation S1

Correspondence to:
P. D. Rosenberg,
p.d.rosenberg@leeds.ac.uk

Citation:
Rosenberg, P. D., et al. (2014), Quantifying particle size and turbulent scale dependence of dust flux in the Sahara using aircraft measurements, *J. Geophys. Res. Atmos.*, *119*, 7577–7598, doi:10.1002/2013JD021255.

Received 26 NOV 2013
Accepted 14 MAY 2014
Accepted article online 16 MAY 2014
Published online 26 JUN 2014

Quantifying particle size and turbulent scale dependence of dust flux in the Sahara using aircraft measurements

Philip D. Rosenberg[1], Douglas J. Parker[1,2], Claire L. Ryder[3], John H. Marsham[1], Luis Garcia-Carreras[4], James R. Dorsey[5], Ian M. Brooks[1], Angela R. Dean[6], Jonathon Crosier[5], James B. McQuaid[1], and Richard Washington[7]

[1]Institute of Climate and Atmospheric Science, School of Earth and Environment, University of Leeds, Leeds, UK, [2]Met Office, Exeter, UK, [3]Department of Meteorology, University of Reading, Reading, UK, [4]Department of Meteorology and the Bert Bolin Centre for Climate Research, Stockholm University, Stockholm, Sweden, [5]National Centre for Atmospheric Science, School of Earth, Atmospheric and Environmental Sciences, University of Manchester, Manchester, UK, [6]Facility for Airborne Atmospheric Measurements, Cranfield, UK, [7]Climate Research Lab, Oxford University Centre for the Environment, Oxford, UK

Abstract The first size-resolved airborne measurements of dust fluxes and the first dust flux measurements from the central Sahara are presented and compared with a parameterization by Kok (2011a). High-frequency measurements of dust size distribution were obtained from 0.16 to 300 μm diameter, and eddy covariance fluxes were derived. This is more than an order of magnitude larger size range than previous flux estimates. Links to surface emission are provided by analysis of particle drift velocities. Number flux is described by a −2 power law between 1 and 144 μm diameter, significantly larger than the 12 μm upper limit suggested by Kok (2011a). For small particles, the deviation from a power law varies with terrain type and the large size cutoff is correlated with atmospheric vertical turbulent kinetic energy, suggesting control by vertical transport rather than emission processes. The measured mass flux mode is in the range 30–100 μm. The turbulent scales important for dust flux are from 0.1 km to 1–10 km. The upper scale increases during the morning as boundary layer depth and eddy size increase. All locations where large dust fluxes were measured had large topographical variations. These features are often linked with highly erodible surface features, such as wadis or dunes. We also hypothesize that upslope flow and flow separation over such features enhance the dust flux by transporting large particles out of the saltation layer. The tendency to locate surface flux measurements in open, flat terrain means these favored dust sources have been neglected in previous studies.

1. Introduction

Atmospheric dust influences the globe, its atmosphere and biosphere, and the human population in a number of ways. It affects the absorption and scattering of radiation in the atmosphere and hence the radiation budget and heating rates. For example, it is known to affect monsoon flows [*Zhao et al*., 2012] and the formation of tropical cyclones over the Atlantic Ocean [*Sun et al*., 2008]. Dust can be transported long distances before being deposited and acting as a nutrient in iron limited environments [*Kaufman et al*., 2005; *McConnell et al*., 2008]. Dust impacts air quality and dust storms can have an economic cost, for example, adversely affecting agricultural land and livestock [*Arnalds et al*., 2001] and causing travel disruption [*Park and Lee*, 2004]. If the dust contains volcanic glass, such as those in Iceland [*Stuart*, 1927; *Arnalds et al*., 2001], then the dust can cause an aviation hazard.

Airborne dust can be identified via satellite, aircraft, or surface observations which may, for example, take the form of imagery, aerosol optical depths, particle size distributions, number concentrations, and mass loadings. These measurements can be used to assess the success of aerosol models predicting uplift, transport, and deposition; however, doing so does not independently test the separate mechanisms of generation, transport, and deposition of dust, which are all dependent upon particle size. Many models have similar aerosol optical depths (AODs) but widely varying emissions [*Huneeus et al*., 2011]. In order to effectively model atmospheric dust, it is important to correctly predict the size-dependent flux of material from the surface into the boundary layer and the free troposphere where it can be transported long distances and have significant atmospheric impact.

In all dust uplift models, two categories of airborne particles are considered, a saltating population and a dust population [*Shao*, 2008]. Saltation particles have diameters $\gtrsim 100\ \mu$m and can be emitted by aerodynamic forces or impacts of other saltators with the surface [*Kok et al*., 2012]. Their motion after ejection is dominated by gravitational forces, and they are expected to exist only in a saltation layer extending a few centimeters from the surface. The dust population contains much smaller and less massive particles which are more difficult to lift via aerodynamic forces due to cohesion forces in the soil. These particles can be ejected by saltator surface impacts and can be lifted above the saltation layer to become suspended for long durations.

Although wind tunnel experiments by *Alfaro et al*. [1997] and the parameterization of *Shao* [2001] indicated the presence of wind speed dependent disaggregation, *Kok* [2011b] found that field experiments [*Gillette et al*., 1972, 1974; *Gillette*, 1974; *Sow et al*., 2009] are not consistent with this finding and suggested the wind speed dependence was an indication that steady state emission was not reached. *Kok* [2011a] provided scale invariant model of dust emission by brittle fragmentation of aggregates of dust particles in the soil which was found to be in excellent agreement with measured emitted particle size distributions.

In this paper we present measurements of the size-resolved dust fluxes retrieved from aircraft measurements throughout the depth of the boundary layer in the heart of the Saharan Desert. These were made as part of the Fennec project. To our knowledge, these are the first measurements of size-resolved dust fluxes to be made from an aircraft. The Fennec project investigated the relationship between dynamics, dust, and radiation in the Earth's deepest boundary layer under the unique conditions of the Saharan heat low [*Cuesta et al*., 2009] and included deployment of eight automatic weather stations [*Hobby et al*., 2013], two supersites [*Marsham et al*., 2013; *Todd et al*., 2013], and 16 flights by the UK's BAe-146-301 Atmospheric Research Aircraft operated by the Facility for Airborne Atmospheric Measurements (henceforth, the FAAM BAe-146).

As the measurements used here are taken from an airborne platform, the derived values do not directly represent surface emissions. However, a number of objectives are achievable from the air, and the aims of this paper are therefore as follows: to (1) provide a detailed methodology of the size-resolved particle flux measurement technique used here with a description of the challenges specific to the platform and the conditions, (2) evaluate the dependence of the flux upon particle size, covering a broader range of sizes than covered in existing literature, (3) evaluate if or how fluxes are affected by different meteorological conditions and regional or local surfaces types, and (4) understand these results in terms of the emission processes which generate the observed dust fluxes.

2. Methods

The dust flux estimates presented here are derived using the eddy covariance method. Details of the instrumentation and methodology are presented below. The use of the aircraft platform permitted measurements in the heart of the Sahara where ground based observations are sparse or nonexistent. It also enabled measurements over a variety of different locations and surface types and allowed us to target meteorological events of interest. However the measurements are made significantly above ground level. The minimum altitude at which the aircraft was capable of safely flying was a function of visibility such that if the pilots were able to clearly see the surface the aircraft was permitted to fly at approximately 100 m above ground level, tracking topography to maintain this altitude. However if at any point the ground was obscured by dust then the aircraft was forced to climb to the local Minimum Safe Altitude defined by maps of the local topography. This was generally of the order 1 km. The finite height above ground of the measurement platform means that the fluxes derived are not directly representative of surface emission; however, the flux measured by the aircraft, which was generally in the lowest 20% of the boundary layer, is clearly strongly related to the emission flux and this relationship is discussed later in the manuscript. In some cases the altitude, combined with a moving platform can be an advantage. For example a single surface flux tower in a hilly region may be biased by its immediate surroundings, whereas an aircraft flying over a hilly region is able to average over many hills and valleys in the varying topography.

2.1. Instrumentation

The FAAM BAE-146 was equipped with a broad range of instrumentation for making in situ measurements of the dust population. Here we use optical particle counters (OPCs), which determine the size distribution of airborne particles via the light scattered from individual particles and optical array probes (OAPs) which image the shadow of larger particles to derive size distributions. *Ryder et al*. [2013b] provides a full list of the instrument suite.

Three particle sizing instruments have been utilized as part of this work on the basis of their reliability and sampling frequency. These are the Passive Cavity Aerosol Spectrometer Probe (PCASP), the Cloud Droplet Probe (CDP), and the Cloud Imaging Probe (CIP) which are an OPC, an OPC, and an OAP, respectively. The PCASP and CDP were found to work well throughout the Fennec detachment, although there may have been a calibration problem with the small sizes measured by the PCASP so the first seven channels (up to ~0.16 μm diameter, all affected by one amplification stage) of this instrument have been omitted as a precaution. In combination these three instruments provide size distributions covering particle diameters ranging from ~0.16 to 960 μm. An important characteristic of these particle sizing instruments is their sampling frequency. The smallest eddy scale which may be captured by the flux derivation is twice the ratio of the aircraft airspeed (approximately 120 m s^{-1}) to the instrument sampling frequency. The PCASP has a sampling frequency of 10 Hz giving a minimum resolvable length scale of approximately 24 m. The CDP gives a 1 ms resolution timestamp for the first 256 particles detected each second (which is sufficient to timestamp every dust particle measured in this work) and the CIP timestamps every one of its images with 0.125 μs resolution. The data from these two instruments were bin-averaged to match the 10 Hz PCASP data.

The CIP was manufacturer calibrated using a spinning disk which passes different sized dots through the laser. Both the PCASP and CDP were calibrated before and after Fennec. In addition the CDP was calibrated on each flying day. Some drift was observed in the PCASP calibrations and the uncertainties used here take this into account. No drift was observed in the CDP calibrations. Because the CDP and PCASP make measurements based upon the optical properties of particles there is a dependence upon the refractive index and shape of the particles. Here these factors are accounted for by assuming spherical particles and Mie theory. The calibrations and the optical property corrections utilize the methods of *Rosenberg et al*. [2012]. The particle refractive index used was 1.53 + 0.001i which gave the best radiative closure between the OPCs and the aircraft nephelometer [*Ryder et al*., 2013b]. When converting from particle diameter to particle mass the equations for the volume of a sphere are used, then multiplied by the product of an assumed density and shape factor ρS. Here we take $\rho S = 2.12$ g cm^{-3} as reported by *Sow et al*. [*Sow et al*., 2009], however we do so noting that it is unclear whether the OPC data upon which this value is derived was corrected for particle refractive index and also that other authors have used different measured or assumed values (e.g., 2.4 g cm^{-3} [*Gillette et al*., 1974] and 2.65 g cm^{-3} [*Tegen and Fung*, 1994]).

For wind measurements, the FAAM BAe-146 utilizes a radome mounted five-port pressure transducer based turbulence probe [*Petersen and Renfrew*, 2009] for angle of attack measurements and a pitot probe for airspeed measurements which allows derivation of aircraft relative 3-D wind vectors. These are combined with data from a GPS inertial navigation unit to provide surface relative winds. This system provides measurements at 32 Hz, although here the data has been resampled to provide 10 Hz data matched to the PCASP. After the campaign it was found that there was a small linear dependence between measured vertical wind speed and aircraft attitude. This dependence was likely caused by a small error in the calibration of a transducer and was removed by subtracting a linear fit.

2.2. Eddy Covariance Flux Measurements

The eddy covariance method has been previously used to derive heat, moisture, and momentum fluxes from aircraft measurements [e.g., *Brooks and Rogers*, 2000; *Petersen and Renfrew*, 2009] and a number of different fluxes including total aerosol number from the ground [*Dorsey et al*., 2002]. Here the same method is used to derive size-resolved dust fluxes using aircraft measurements. To do so the vertical wind and dust number or mass concentration are separated into a mean value and a deviation from the mean by way of Reynolds decomposition. When applied to dust measurements the appropriate decompositions are

$$p(t) = \overline{p} + p'(t), \tag{1}$$

where p is a placeholder for vertical wind component, w, dust number concentration, n, or dust mass concentration, m. Barred symbols represent the mean over a fixed time period and dashed symbols represent the perturbation from the mean over the same period. The flux of n is then related to the covariance of n and w such that

$$F_n = \overline{w'(t)n'(t)}, \tag{2}$$

with an equivalent equation for dust mass concentration, m. In this work we perform a linear detrend of the data before the Reynolds decomposition and we time-shift the concentration data by a small amount (less than 1 s) in order to account for position offsets of the instruments along the airframe and maximize the cross correlation with the winds. Detrending reduces contamination of the turbulent flux estimate by mesoscale variations. Because material that has been transported long distances will be well mixed within the boundary layer, it will provide small values of $n'(t)$, which will not be correlated with $w'(t)$ so will provide negligible flux contributions. However, due to the height of the measurements, some dust transport will occur before the measurements are made. This will certainly affect the magnitude of the dust fluxes measured and have the potential to affect the largest sizes which may succumb to gravitational settling.

Some limitations to the eddy covariance method are particularly relevant to the aircraft platform and the Saharan boundary layer. High-frequency measurements are required so that small eddy scales are sampled. As the aircraft is traveling at approximately 120 m s^{-1} and the instrument sampling period is 0.1 s, we only sample eddies with sizes $\gtrsim$ 24 m. It is also of note that turbulent scales are likely to be larger at the aircraft altitude than at ground level. The flight leg over which one flux derivation is made must be long enough to span multiple eddies at the largest eddy scales and to provide sufficiently good counting statistics for the dust measurements. As the Saharan boundary layer can be 5 km deep and the mass concentration may be dominated by a relatively small number of large particles, this can require legs of 50–100 km. Finally, the measurement area should be homogeneous or at least mesoscale variations should be linear with distance. It is clear that there is a trade-off between these requirements as longer legs are more likely to encounter mesoscale variations. In order to achieve the best flux estimates the following principles have been followed. The flight data has been carefully selected to avoid mesoscale variation where possible. Care has been taken to derive rigorous uncertainties for the dust flux measurements. Where these are high, size-resolved estimates have not been utilized.

In order to ensure that both the largest and smallest eddy scales have been measured we plot an ogive curve for each flux leg [*Brooks and Rogers*, 2000]. The ogive is the cumulative integral of the cospectral density, so it is steepest for eddy scales which make a large contribution to the flux. The cospectrum is not used directly because it is noisy, making it difficult to identify the contributing length scales. The integration performed to create an ogive quickly provides a signal which is larger than the noise and the signal to noise ratio continues to improve along the curve. This means an ogive can be usefully plotted on a linear vertical scale and the ogive has therefore become the defacto standard for analyzing scale dependence of fluxes. If the turbulence is well behaved and all relevant length scales are measured, the ogive should be flat at both ends (the largest and smallest scales) where contributions to the flux are negligible. Here all ogives are normalized to unity at the largest length scales.

One potential problem with measurements of particle fluxes is the nonnegligible mass of large particles. There is therefore a downward flux of particles caused by gravitational settling and a deviation of particle velocities from the atmospheric turbulent motion. The fluxes here exclude gravitational settling as this is a deposition process assessed separately in models and the flux from this process is additive. However, we do require a framework to assess the importance of particles not following turbulent motion, which we derive as follows. Considering a stationary particle which is exposed to an eddy of diameter s providing an updraft speed w, the air traverses the eddy in a time $t \approx s/w$, by which time the particle lags the air by a distance

$$\Delta s = w\tau(1 - \exp[-t/\tau(d)]), \tag{3}$$

where $\tau(d)$ is the aerosol relaxation time as a function of its diameter as per the standard definition for this parameter. The average speed of the particle over this time is then given by $(s - \Delta s)/t$. The inertial correction factor is simply the ratio of the mean particle velocity to the air velocity which, from the above, is found to be

$$c_{in} = 1 - \frac{1 - \exp(-R)}{R}, \tag{4}$$

where we define R as the particle-eddy interaction parameter given by $s/(w\tau(d))$. Physically, the eddy influence can be considered as the dimensionless aerodynamic impact that an eddy has upon the trajectory of an aerosol particle. As R increases from zero the turbulent motion has an increasing effect upon the particle trajectory. As one would expect, R increases with increasing eddy size and decreasing particle relaxation time (and hence mass) and vertical velocity. c_{in} approaches unity asymptotically as R increases and is zero when the eddy

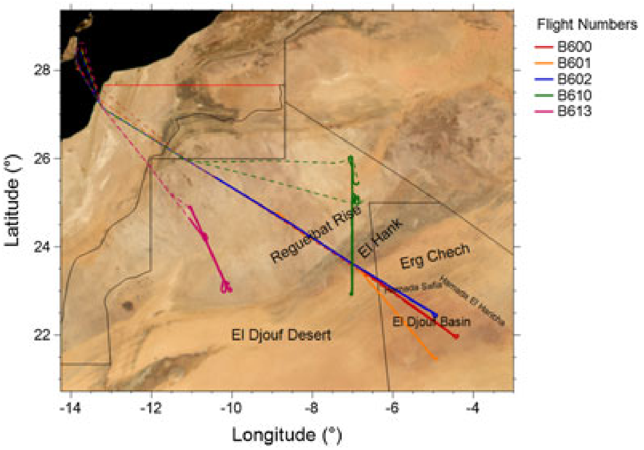

Figure 1. Aircraft tracks overlain upon cloud filtered satellite imagery [*Reto et al.*, 2005] labeled with geographical features of note. Bold lines show aircraft tracks below 6.0 km in the area of interest, and fine dashed lines show tracks for higher altitude flying, takeoffs, and landings. The overlain northern endpoints of the low-level tracks of B600 and B601 are within 0.5° of the northern endpoint of the visible B602 low-level track.

influence is zero. For values of R greater than 20, c_{in} is greater than 0.95. As will be discussed later in this paper, c_{in} is always close to unity for the measurements presented here and is therefore neglected.

2.3. Satellite and Model Products

In order to effectively interpret the results, data from the Meteosat Second Generation mounted Spinning Enhanced Visible and Infrared Imager (SEVIRI) red-green-blue thermal infrared dust product and Operational forecasts from the Met Office Africa Limited Area Model (Africa LAM) were used. These allow the data to be placed in wider scale context. The SEVIRI dust product images presented here show dust as a bright pink color [*Brindley et al.*, 2012]. However, the surface is similarly colored to the dust in some locations and the dust-surface contrast depends in part upon temperature contrast and therefore dust height. The dust becomes much more obvious in animations where it can be seen to move against the stationary background. The Africa LAM is a regional simulation using the Met Office Unified Model (UM) [*Lock et al.*, 2000; *Davies et al.*, 2005] and has a 12 km horizontal grid spacing at the equator and 70 vertical levels. Here it is used to provide estimates of near surface horizontal wind.

2.4. Uncertainty Calculations

Because of the discrete nature of the particle measurements, counting uncertainty represents a significant contribution to the total uncertainty of the particle concentration and hence flux. When considering mass flux, this is often the dominant uncertainty source. The contribution by all random uncertainties, including counting uncertainty and noise in the turbulent velocity data, can be assessed by the method described by *Billesbach* [2011]. To do so, the concentration measurements are shuffled, which provides a data set that is uncorrelated with the vertical winds but follows the same probability density function as the unshuffled data. The standard deviation of the cross correlation series of the shuffled data with the vertical winds is equal to the noise level and hence the random uncertainty. The other major contributor to the dust mass flux is the derivation of the mass per particle. As discussed above this is a function of the uncertainties in particle optical properties, shape, and density and generates a systematic uncertainty which is likely to be of the order 25%.

3. Synoptic and Geographic Background of the Observed Dust Uplift Cases

Sixteen flights were carried out during Fennec in 2012, eleven of which included measurements in the heavily dust laden boundary layer. Dust flux measurements from five flights are presented here. These flights were chosen because the flight patterns used and the conditions observed permitted measurement of statistically significant dust fluxes. The tracks of these five flights, along with their flight reference numbers are shown in Figure 1; flight times, locations, and observed conditions are summarized in Table 1. Also labeled on Figure 1 are geographical features which influence dust uplift in the region.

Geography clearly has a significant impact upon dust uplift, for example, by orographic channeling of winds, which has previously been implicated in erosion on various scales [*Washington et al.*, 2006; *Netoff and Chan*, 2009], and by determining availability of erodible material [*Schepanski et al.*, 2013]. The descriptions here are based on in-flight observations, satellite imagery, the Africa AMS Topographic Map Series, and information from Mauritanian colleagues. Regueibat Rise is an elevated region of bright terrain in northern Mauritania. It is

Table 1. Summary of Flights for Which Dust Fluxes Have Been Derived

Flight Number	Date	Entered Area of Interest (UTC)	Left Area of Interest (UTC)	Altitude Range Above Surface[a] (m)	AOD[b]	Conditions	Location
B600	17/6/2011	10:10:00	11:12:35	680–800	2.24	Harmattan wind with LLJ features breaking down during the day	Regueibat Rise, El Hank, Erg Chech, El Djouf Basin
B601	17/6/2011	16:57:00	18:19:03	720–820	3.08		
B602	18/6/2011	10:18:08	11:27:27	110–70	1.07		
B610	25/6/2011	08:57:22	10:39:33	60–150	0.52, 1.75	Narrow LLJ	Regueibat Rise, El Hank, Erg Chech
B613	26/6/2011	15:17:47	17:31:16	70–4300	0.55, 0.55	Stacked legs in light wind after LLJ breakdown	Regueibat Rise

[a] Measured by a radar altimeter (surface referenced) for heights below 2000 m or by GPS (ellipsoid referenced) above 2000 m. Only heights where fluxes were measured are included.

[b] Aerosol optical depth at 550 nm (AOD) was derived by integration of aircraft measurements during profiles between the transit altitude (~8 km) and the lowest flight level. The first measurement for each flight was made as the aircraft entered the area of interest, and the second value (where available) was made as the aircraft left the area of interest.

relatively flat with some shallow broad drainage channels running across the surface. A line of dunes penetrate the region from the northeast. Very sparse low scrub was observed over the region, particularly in preserved vehicle tracks, implying that the surface has a low erodability. Regueibat Rise is bordered to the south by a dark series of linear ridges and waddis known as El Hank. The dried up drainage channels here provide a source of loose material and potential for channeling of winds. Some bright mineral deposits in dried lake beds were also observed here. Immediately to the south of El Hank is the Erg Chech sand sea which then blends into the El Djouf Desert. The Erg Chech dunes are oriented approximately NE with spacings of ~1–10 km. Between the dunes, nonsandy dark surface is visible, as are some bright dry lake beds. In Mali at the north-eastern edge of El Djouf is a basin bordered to the north and east by ridges known as Hamada Safia and Hamada El Haricha. Close to Erg Chech, the El Djouf Basin also consists of sand sea, but with closer spaced dunes. Moving southward the dunes become sparser and disappear. All these regions were overflown by the FAAM BAe 146 during Fennec, providing data over sand seas, dry river and lake beds, stable soil, and steep and shallow terrain.

The meteorology of all five flights was influenced by nocturnal low-level jets (LLJs). LLJs are formed in this region when deep dry convection halts in the evening, reducing downward momentum transport and therefore reducing the impact of friction upon the lower boundary layer. The resulting force imbalance causes an oscillation about the new equilibrium point, creating a supergeostrophic jet at altitudes of approximately 500–1000 m [*Blackadar*, 1957; *Van de Wiel et al.*, 2010]. After sunrise dry convection resumes, mixing the momentum of the jet down towards the surface, which increases both mean wind speed and gustiness [*May*, 1995; *Knippertz*, 2008]. This plays an important role in dust uplift due to the nonlinear relationship with the friction velocity. LLJs are a common feature in the Sahara in Summer [*Fiedler et al.*, 2013; *Marsham et al.*, 2013; *Todd et al.*, 2013]. *Schepanski et al.* [2009] found that 65% of satellite observed dust emission events occur in the 0600–0900 UT period consistent with the time of LLJ breakdown, however this can be regarded as an upper estimate as other dust uplift mechanisms are associated with clouds, prohibiting satellite identification [*Heinold et al.*, 2013; *Kocha et al.*, 2013]. Here, LLJs have simply been identified from the Africa LAM as morning peaks in wind speed between the surface and 1500 m altitude around the Saharan heat low which mix away during the day. The fact that all flights presented here are related to LLJ dust uplift does not imply that these are the dominant dust uplift mechanism in the region. The synoptic scales of LLJs make them relatively easy to forecast, easy to target with flights and easy to collect data under homogeneous conditions. In contrast dust uplift events caused by cold pool outflow from mesoscale convective systems, known as haboobs, cannot be easily forecast by models with parameterized convection [*Marsham et al.*, 2011]. This makes them difficult to target. They also exhibit significant heterogeneity [*Solomos et al.*, 2012] making flux derivations difficult.

Three of the five flights (B600, B601, and B602) occurred on 17 and 18 June 2011 and each followed a very similar flight track. The meteorology on these two days was also similar, with the Africa LAM forecasting a broad scale Harmattan Wind linked to a LLJ flowing from Algeria into northern Mauritania and Mali as seen in Figure 2. On the morning of 17 June, the wind speed was above 7 m s^{-1} up to 3 km, with a 16.5 m s^{-1} maximum at 1 km. On the 18 June, a similar wind maximum at 1 km and a second wind maximum at 3 km

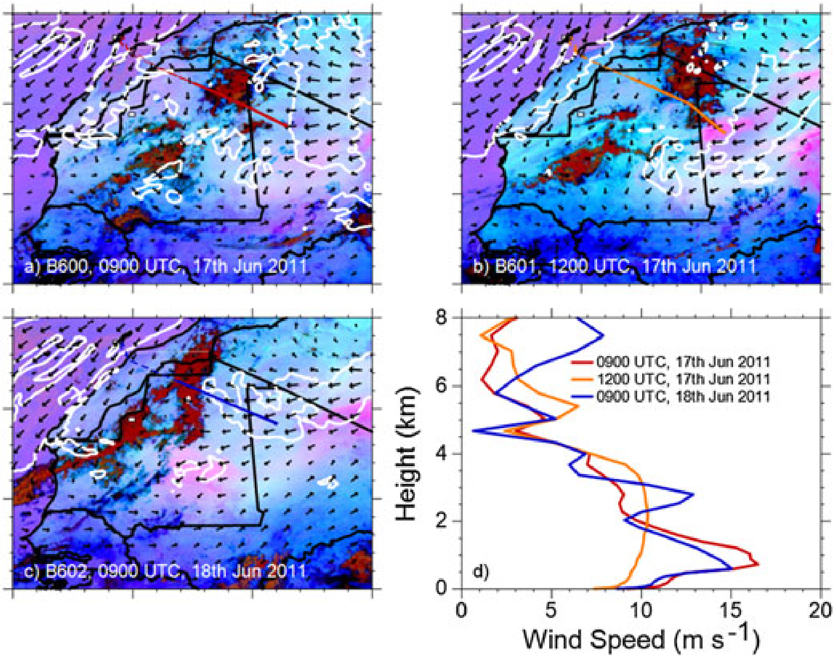

Figure 2. False color SEVIRI images for (a) 0900 UTC and (b) 1200 UTC from the 17 June 2011 and (c) 0900 UTC on the 18 June 2011 overlain with wind vectors forecast by the Africa LAM operational model on its lowest level (10 m). The white contour is at 8.0 m s^{-1}. Colored lines show aircraft tracks as in Figure 1. Dust is evident as a pink color and can be seen to form a band stretching from Algeria to the Mali/Mauritania border during 17 June 2011 corresponding to regions of high forecast winds. (d) The forecast wind profiles at the most SE point of the aircraft track at the same times as Figures 2a–2c.

were forecast. In contrast, the forecast for midday on 17 June shows a much more well-mixed profile. The aerosol optical depth at 550 nm (AOD) measured during the descent was much lower for flight B602 (Table 1). The three flights all consisted of a high level transit followed by descent to the minimum permitted altitude at the farthest southeast point, then a return to the northwest at low level. During flights B600 and B601, visibility was poor close to the surface, and the low-level legs were at altitudes of between 700 and 800 m. However, the aircraft was able to descend briefly to 500 m during B601. During B602 visibility was better and the low-level leg was performed at 100 m above the ground.

Flight B610 probed the decay of another forecast LLJ on 25 June 2012 over northeast Mauritania during the period just after dawn as seen in Figure 3a). Two reciprocal low-level legs were performed at the expense of covering a smaller geographic region than during flights B600-B602. Visibility permitted these legs to be made at 100 m above ground level. Again an upper level (4 km) wind maximum was forecast and observed by the aircraft in addition to the 18 m s^{-1} LLJ maximum as seen in Figure 3b. This time the LJJ was less geographically expansive and further north, encompassing the El Hank and Regueibat Rise regions.

The final case considered here is flight B613 which consisted of a series of stacked legs in the boundary layer in the afternoon of 26 June. This flight was at the far western extent of an east-west LLJ identified in the 0900 Africa LAM forecast (not shown). At the flight location the 0900 forecast indicated two low-level wind maxima (not shown), both of which were weaker than those forecast for the previous cases. The first was of 10 m s^{-1} at 1200 m altitude and the second of 7.5 m s^{-1} below 500 m altitude. The winds at the flight time were forecast to be only 3 m s^{-1} on the lowest model level and well mixed throughout the boundary layer as shown on Figures 3c and 3d. The measurements indicated a slightly larger mean wind speed than forecast and also a positive gradient in wind speed with altitude which was not forecast. The gustiness of the wind was particularly notable in this case with 5–10 m s^{-1} peak-to-peak variations of the wind speed within the boundary layer. Because dust uplift is highly nonlinear and is generally modeled as being proportional to wind speed cubed once the wind speed has exceeded a threshold, this gustiness is important for potential dust uplift.

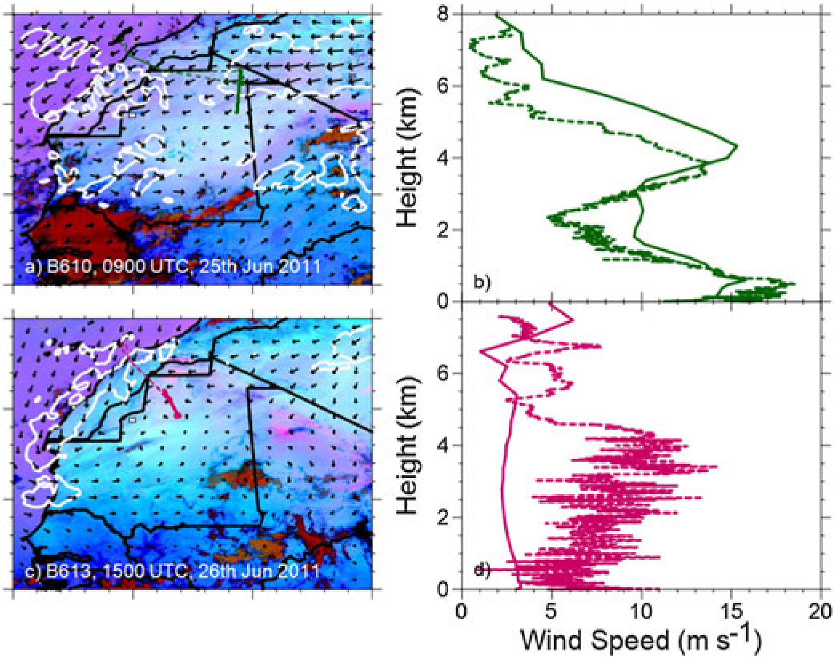

Figure 3. (a and c) Images show false color SEVIRI images overlain with forecast Africa LAM wind vectors and the white 8 m s^{-1} contour as per Figure 2, for times corresponding to flights B610 and B613. Colored lines show aircraft tracks as for Figure 1. (b and d) Images show forecast Africa LAM wind profiles at the same times as Figures 3a and 3c, respectively, with corresponding measured wind profile from the aircraft descents.

4. Results and Discussion

The results presented here include both size-resolved and total fluxes. We first present the size-resolved results, then discuss how this size-resolved data can be used to link the flux to surface emission. We then present the total fluxes derived by integration of the size-resolved data and a flux profile. Finally we discuss the effects of large particles not following streamlines.

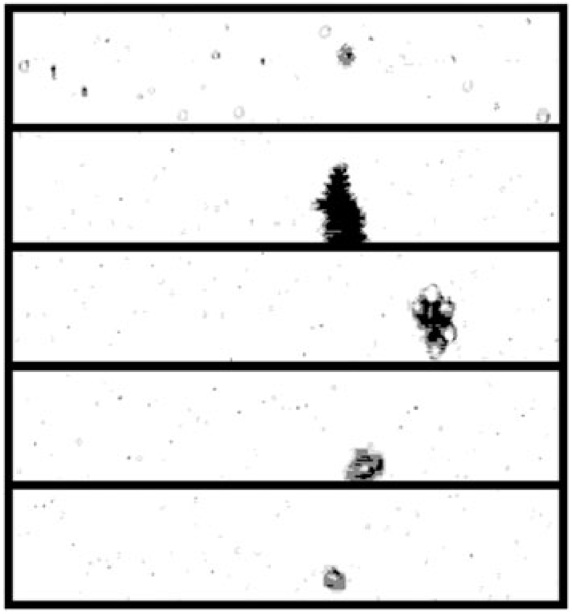

Figure 4. Example images of large dust particles collected by the CIP15 probe during flight B601. The image resolution is 15 μm, and the height of each strip is 960 μm. Note that the CIP only records pixels when a particle is in the field of view so horizontal spacing in the images is not representative of actual particle spacing.

4.1. Size-Resolved Fluxes

The size-resolved nature of the measured dust concentrations enables derivation of size-resolved dust fluxes for the flight legs where signal to noise was highest. This was the case for 18 sections of flights B600, B601, B602, and B610. The set of instrumentation, uniquely used to measure dust onboard the FAAM BAe 146, has enabled dust fluxes to be derived over a size range more than an order of magnitude wider than previous published data sets. Analyses of the size distributions themselves are presented by *Ryder et al.* [2013b]. Unique in this case was the use of an OAP for measuring dust particles and some example images showing the largest measured particles are presented in Figure 4.

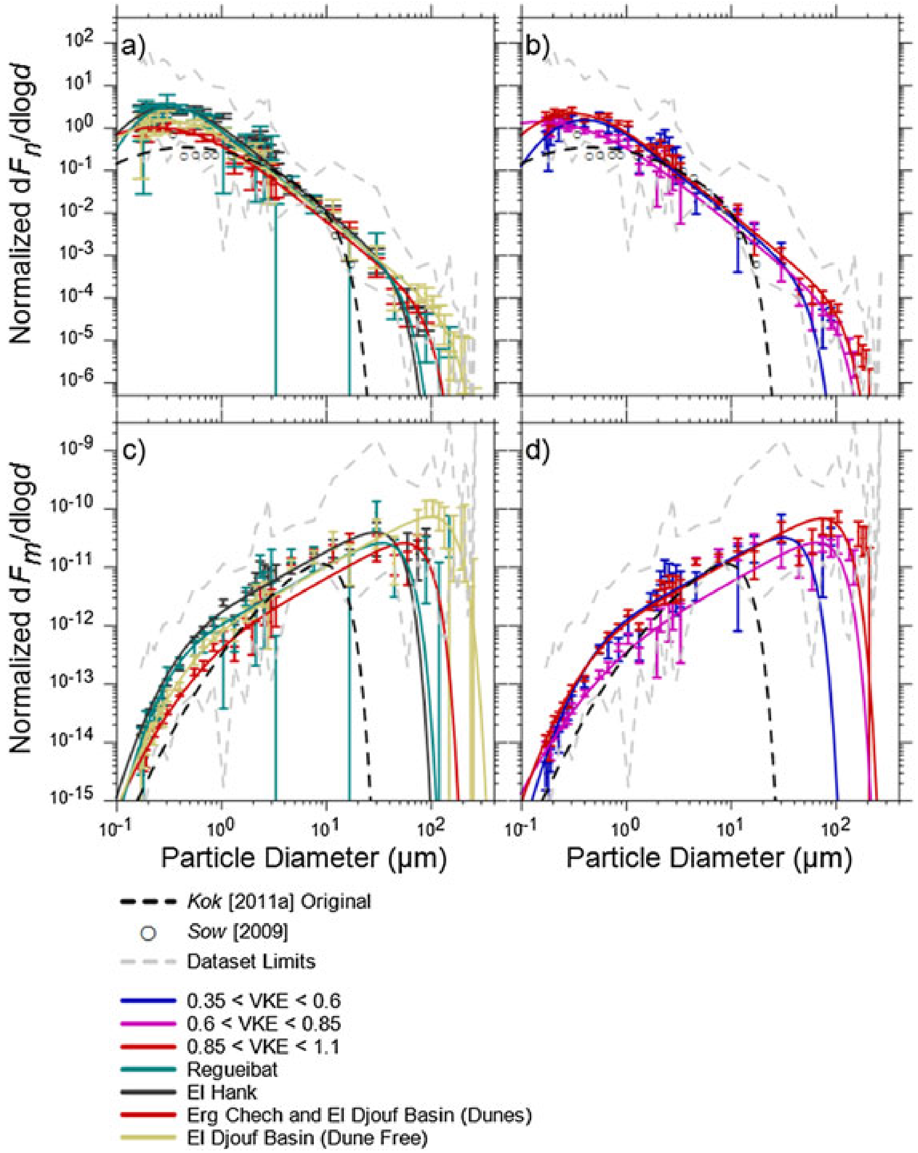

Figure 5. Size-resolved number and mass fluxes from flights B600, B601, B602, and B610. All plots show the gray dashed line, which indicates the range of all positive dust fluxes measured during the flights, and the black dashed curve, which is the unaltered *Kok* [2011a] parameterization. Open circles are the measurements by *Sow et al.* [2009]. Colored curves represent the same parameterization but fitted to the measurements, shown in the same colors. (a and c) Eeach colored curve represents the average flux distribution for different ranges vertical turbulent kinetic energy (VKE). Units of VKE in the legend are $m^2\ s^{-2}$. (b and d) Each curve represents the average flux distribution measured over a different geographical region. Measurements with uncertainty larger than 100% have been omitted from the plots for clarity.

Kok's [2011a] brittle fracture theory predicts that the measured flux as a function of size is controlled by cracks which split and merge during excavation of soil by saltator impacts.

$$\frac{\mathrm{d}F_n(d)}{\mathrm{d}\log(d)} \propto d^{-2}\left\{1+\mathrm{erf}\left[\frac{\ln(d/d_s)}{2\ln(\sigma_s)}\right]\right\}\exp\left[-(d/\lambda)^3\right] \tag{5}$$

where $F_n(d)$ is the size-resolved number flux, d is particle diameter, λ is the scale length representing the penetration distance of secondary cracks, and d_s and σ_s are the geometric mean and standard deviation of the soil particle size distribution, respectively. Transformation of (5) can easily be performed to give a similar function for the size-resolved mass flux, F_m. (5) is the product of a power law, a soil function and a scaling

Table 2. Soil Related Best Fit Parameters for Different Overflown Regions

Region	d_s (μm)	σ_s (μm)
El Hank	0.46 ± 0.06	1.8 ± 0.2
Erg Chech and El Djouf Basin (dunes)	0.78 ± 0.2	2.5 ± 0.3
El Djouf Basin (dune free)	0.61 ± 0.09	2.1 ± 0.2
Regueibat	0.38 ± 0.05	1.6 ± 0.2

function. The power law is predicted by brittle fracture theory. The soil function represents the indivisible nature of the fully dispersed soil and causes a reduction in flux at small sizes. *Kok* [2011a] suggested that a single set of values for the two soil parameters ($d_s = 3.4$ μm, $\sigma_s = 3.0$) is consistent with all available dust flux data. The scaling function is chosen to be of a functional form which fits the data; generally an exponential is used [*Åström*, 2006]. The scale length used by *Kok* [2011a] was 12 μm, which was empirically derived by fitting to available flux data. The scale length and soil parameters used by *Kok* [2011a] provided a flux distribution which followed a power law in the diameter range 2–10 μm with lower fluxes for smaller and larger diameters. *Kok* [2011a] stated that all existing size-resolved flux data were compatible with a single set of values for λ, d_s and σ_s.

When comparing our results to (5) we group data according to properties which may influence the flux. In one case we group data by terrain type to test for differences in the soil parameters and in another case we group data according to vertical turbulent kinetic energy (VKE) $= \overline{w'^2}/2$ to test for transport effects. We do not attempt to group by wind speed as we have no way to determine surface wind speeds from our measurements at altitude. The grouped size-resolved fluxes, normalized over the 2–10 μm range, are presented in Figure 5. Also shown on Figure 5 is (5) using the original *Kok* [2011a] parameters and (5) fitted to the data sets using d_s, σ_s, and λ as free parameters.

The aircraft data near the center of the distributions fit within their spread to the −2 power law predicted by (5). Because the measurements were made at 60–800 m altitude this result indicates that processes such as advection or vertical transport have not modified the shape of the flux distribution for these sizes. The original parameterization fits the data well over the 2–10 μm diameter normalization range where *Kok* [2011a] suggested the flux should follow a power law. However, the large particle size cutoff at ~20 μm in the parameterization is not seen in the observations. The extension of the power law beyond 20 μm is somewhat surprising given that particles larger than this diameter can be lifted directly by aerodynamic forces or particle splash [*Kok et al.*, 2012]. Hence, we might not expect the brittle fragmentation mechanism to correctly predict the size-resolved flux of loose particles above this size. If, however, these particles are aggregates made of material which was bound within the soil, then we would expect the brittle fracture mechanism to apply. The scale invariance of the brittle fracture mechanism predicts that large aggregates will be created provided that the scaling parameter is sufficiently large. The images presented in Figure 4 show at least one particle which can be identified as a large aggregate despite the 15 μm resolution.

At the small sizes, we again see an extension of the power law beyond the original parameterization. Best fit values for the soil parameters which control the curve at small sizes are given in Table 2. In all cases, the geometric mode is significantly smaller than that given in the original parameterization of 3.4 ± 1.9 μm. We also see differences between the different emission locations. Dune covered terrain provides the lowest relative flux of small particles and the crusted terrain provides the highest relative flux of small particles. The dust flux over Regueibat is fitted by the smallest values of the soil parameters, whereas that over the El Djouf Basin dunes is fitted by the highest values of the soil parameters. These variations are consistent with the expectation that crusted terrain consists of a fine soil particles giving stronger cohesive forces and that dunes consist of coarse soil particles giving low cohesion. The impact of these differences is that the dust flux over the crusted surface of Regueibat follows a power law to smaller diameters than over El Djouf Basin dunes. The different VKE ranges show less variability for small particles than the different terrain categories and there is no clear correlation between the best fit soil parameters and VKE as can be seen in Table 3. The results of *Sow et al.* [2009] show some deviations from our result similar to those of the [*Kok*, 2011a] parameterization. This is not

Table 3. Soil Related Best Fit Parameters for Different Values of VKE

Region	d_s (μm)	σ_s (μm)
$0.35 < \text{VKE} < 0.6$	0.54 ± 0.09	1.8 ± 0.2
$0.6 < \text{VKE} < 0.85$	0.74 ± 0.2	2.7 ± 0.5
$0.85 < \text{VKE} < 0.10$	0.53 ± 0.07	2.0 ± 0.2

surprising given that this data set was use in the tuning of the parameterization. We note however that the *Sow et al*. [2009] data show an increased flux at its smallest size. This data point is in better agreement with the measurements presented here than the four points which follow.

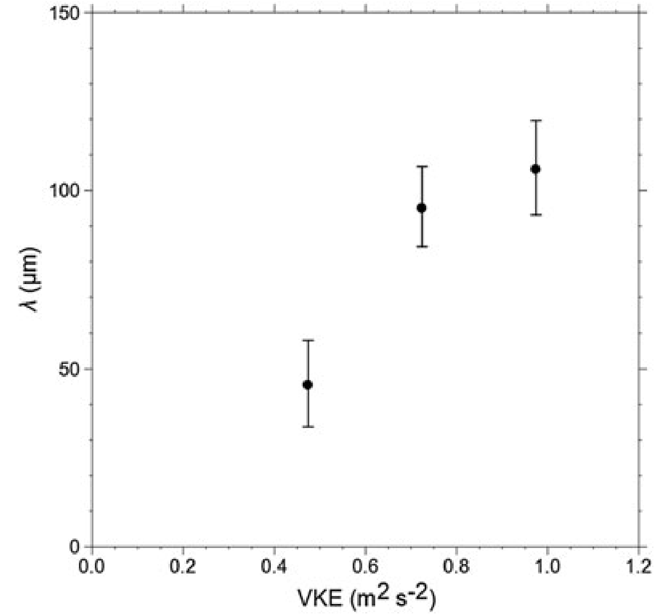

Figure 6. Variation in the parameter λ for the fits in Figures 5a and 5c as a function of VKE.

The large particles, from 5 μm up to 300 μm dominate the mass flux, contributing 90%. They are ubiquitous in the flux measurements and are not limited to the higher dust loading events. They include particles that would usually be categorized as saltators and not be expected to leave the saltation layer within a few cm of the surface. Although cohesive forces are low for large particles and they can be emitted via direct aerodynamic uplift or via a splash mechanism [*Kok et al*., 2012], we see in Figure 5 that the flux distribution for these large particles can be effectively modeled by the brittle fracture parameterization if λ is increased sufficiently. Because of poor counting statistics at the larger sizes the uncertainties are large. However the curves for the highest VKE in Figures 5a and 5b extend to larger diameters than the curves for lower VKE. This indicates an influence of vertical transport upon the maximum particle size for which a positive flux occurs. Figure 6 shows how λ varies for the three different VKE categories. A clear correlation is seen, consistent with the hypothesis that VKE affects the particle size range over which the dust flux occurs. It is not sufficient, however, to prove a causal link. VKE could, for example, be correlated with peak horizontal winds and hence saltator impact velocities. However, the impact of wind speed upon size distribution is disputed [*Alfaro et al*., 1997; *Kok*, 2011b]. If, however, VKE is regulating the flux through transport then the physical interpretation of λ shifts from being related to the brittle fracture process itself to being a limit imposed by the dynamics of vertical mixing. This would mean that the maximum diameter of dust emitted into the boundary layer is limited by vertical transport and is independent of the emission mechanism. It is not surprising that the exponential cut-off term in (5) can describe both processes, as it is often used as a proxy for a number of particle size limiting processes in brittle fracture parameterizations [*Åström*, 2006].

To date, no other studies have observed fluxes of such large particles and we suggest some hypotheses here to explain this discrepancy. The first possibility is measurement bias. Large aerosol particles are difficult to measure because they are found in low concentrations and tend to be lost to gravitational settling and inertial impaction inside instrument inlets and pipes. *Sow et al*. [2009] reported a cut-off diameter of 40 μm for their sampling system and reported size-resolved data up to diameters of 15 μm. Detections of larger particles were too infrequent for use. *Gillette et al*. [1972] collected particles on a silicone oil covered slide and reported results up to 12 μm diameter. By comparison the FAAM BAe 146 is equipped with open path instrumentation for particles above 3 μm diameter, so avoid sampling system losses. This ensures that the maximum measured diameters are limited only by the scarcity of large particles. A second explanation could be that the large mass and terminal velocity of these particles makes it difficult for them to be lifted out of the saltation layer. So close to the surface turbulent eddies are limited in their scale so cannot generate the ~0.1–2.0 m s^{-1} vertical wind velocities needed to suspend these particles. However upslope winds can generate vertical velocities of this magnitude and flow separation at slope peaks can inject the particles to heights of tens or hundreds of meters. Once at these heights, the intense turbulence generated over the Sahara can mix the particles throughout the boundary layer. At 100 m above the Saharan surface, the aircraft typically measured ±4 m s^{-1} peak vertical wind speeds. The slopes involved could be hill and valley systems

[*Egan*, 1984] such as those found at El Hank or dunes [*Schatz and Herrmann*, 2006] such as found in Erg Chech. The tendency to mount instrumentation away from such features to avoid contamination of results [*Gillette et al.*, 1974; *Sow et al.*, 2009] will have resulted in such an injection mechanism being missed.

The impact of these large dust particles is restricted to the local region. They have terminal velocities of the order 1 m s^{-1} and hence even when mixed to 5 km altitude they will settle to the surface overnight, although shear driven turbulence or lifting from haboobs are able to keep large particles aloft longer [*Ryder et al.*, 2013a]. Despite the fast settling, large particles may have a significant local impact on air quality, visibility, radiative balance, and cloud processes. Because the dust is so large, it will act as cloud condensation nuclei (CCN) [*Koehler et al.*, 2009] and even as a Giant CCN. If uplift of such large dust particles is found to exist beyond just the Sahara, then other large human populations will be affected. There will be an impact upon estimates of increased melt rate of glaciers and seasonal snow packs due to dust deposition which has both distant [*Sodemann et al.*, 2006; *Painter et al.*, 2007] and local moraine [*Oerlemans et al.*, 2009] sources. There will also be an impact upon estimates of uplift from soils containing volcanic material, for example in Iceland [*Stuart*, 1927; *Arnalds et al.*, 2001] (i.e., resuspended volcanic ash) where aircraft and surface observations have shown significant uplift [*Blechschmidt et al.*, 2012; *Prospero et al.*, 2012]. Such uplifted dust is likely to present a similar aviation hazard to volcanic ash [e.g., *Prata and Tupper*, 2009; *Drexler et al.*, 2011].

4.2. Flux Source and Drift Velocity

Although surface emission is the initial source of dust, once it has been lifted other nonemission processes may affect the flux, including, particle settling, entrainment and differential advection. Particle settling causes particles to become concentrated in the lower atmosphere and generates a concentration gradient. Vertical mixing across this gradient generates a flux which counters the gravitational settling. Entrainment at the boundary layer top generates a flux because the air above the boundary layer generally contains a different (usually lower) concentration of dust to the boundary layer itself. Boundary layer growth and entrainment generates a concentration gradient and mixing across this again generates a flux. Finally, differential advection can bring together air from different source regions at different altitudes, this air may have different dust concentrations and again mixing across this concentration gradient generates a flux. We mostly expect that flux due to differential advection will be low, because the boundary layer is well mixed and above the surface layer we expect the wind to be approximately constant.

It is possible to distinguish between fluxes generated by emission and these other mechanisms by considering the drift velocity of the dust (also referred to as emission velocity for direct measurements of emission) [*Dorsey et al.*, 2002]. Drift velocity is given by $v_d(d) = F_n(d)/n(d)$, and the relationship between $v_d(d)$ and the gravitational settling velocity, $v_s(d)$, is different for each case. In the case where we have a flux generated only by gravitational settling, we expect to see either a balanced system where $v_d \approx -v_s$ or an unbalanced system where previous emission has not yet reach equilibrium and hence $v_d < -v_s$. These comparisons apply for all diameters. Where we have a flux due to entrainment of clean air v_d is larger than v_s and as the concentration of particles becomes diluted v_d increases further and hence we expect $v_d \geq -v_s$ for all diameters. The increase in v_d should be particularly large for large particles which are particularly scarce above the boundary layer. For flux due to differential advection, we expect no particular relationship between v_d and v_s and may find that v_d is negative. Finally, for emission v_d is initially larger than v_s. However, as the concentration of particles increases, v_d decreases until the atmosphere saturates for a given particle diameter, giving $v_d \approx -v_s$. Because the magnitude of v_s increases with d^2 and because (5) predicts that for particles larger than 1 μm flux decreases as d^{-2} or faster, we expect that large particles will reach a balance with gravity much sooner than small particles. Hence, for emission we should find that a saturation diameter, d_{sat}, exists such that $v_d(d) > -v_d(d)$ for $d < d_{sat}$ and $v_d(d) \approx -v_d(d)$ for $d > d_{sat}$.

Figure 7 shows measured drift velocities and calculated settling velocities as a function of diameter for the peak flux measurements of flights B600, B602, and B610. Settling velocities were derived assuming standard surface conditions for deriving atmospheric density and viscosity. Settling velocities deviate from a power law at large sizes due to the transition to turbulent flow around the particles, which are assumed to be spherical. We see that smaller particles have $v_d >> -v_s$ and for larger particles $v_d \approx -v_s$. This is consistent only with the recent local uplift scenario, it is not consistent with balancing of flux with gravitational settling

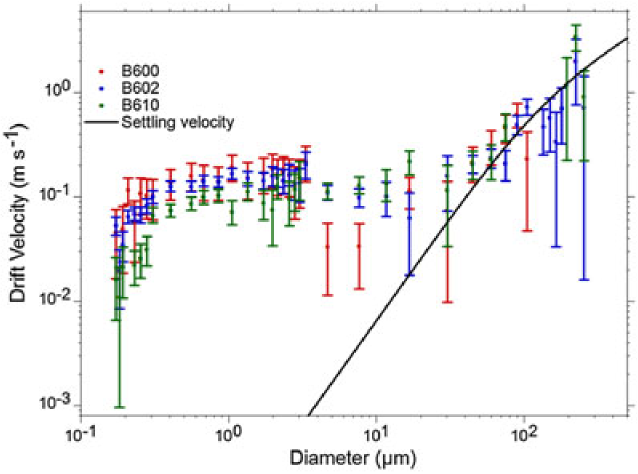

Figure 7. Drift velocity as a function of particle diameter for the peak flux measurements of flights B600, B602, and B610. Points with uncertainties greater than 100% have been omitted. Data from Flights B601 and B613 are not shown due to their low fluxes. The line shows an estimate of the particle settling velocity. Drift velocities and settling velocities are both given positive signs for comparison despite their opposite directions.

of particles having undergone long range transport, nor with entrainment of clean air at the boundary layer top. Although we cannot absolutely rule out that the flux is due to differential advection, it seems highly unlikely that in all three of these cases the same pattern would be generated by this mechanism. Of course some horizontal transport of the measured particles must have occurred, as they require a finite time to mix up to the altitude of the aircraft. However, this analysis indicates that the transport time is significantly smaller than the time required to mix emission through the boundary layer. The strong updrafts of a few meters per second measured in the boundary layer would be expected to perform such mixing on time scales of the order one hour, leading to the conclusion that emission must have occurred within a few tens of km of the measurement location.

4.3. Total Number Fluxes and Mass Fluxes

4.3.1. B600, B601, B602 Broad Harmattan LLJ

Figure 8 shows measured surface and atmospheric parameters as well as the number and mass fluxes derived for the three broad scale Harmattan LLJ flights: B600, B601, and B602. To the south, where the LLJ was forecast to be strongest, the dust number and mass concentrations tended to be the highest. The B600 and B602 flights occurred in the morning closer to the expected time of LLJ breakdown. In these cases, highly variable regions of dust concentration were associated with peak dust fluxes towards the south of the legs and nearest to the forecast LLJ position. Further north, the dust concentration was lower and less variable, but with a few spikes in concentration which may represent small uplift events. These two flights also showed the largest dust fluxes which peaked to the south, with values of $(1.2 \pm 0.40) \times 10^7$ m^{-2} s^{-1} and 0.37 ± 0.18 mg m^{-2} s^{-1} for B600 and $(1.6 \pm 0.17) \times 10^7$ m^{-2} s^{-1} and 0.20 ± 0.051 mg m^{-2} s^{-1} for B602. The uncertainty of the B600 peak is large because quickly varying conditions along the flight track limited the integration time to only 300 s, compared to 700 s for the B602 peak. The B600 and B602 flux maxima were recorded at the southern and northern perimeter of the El Djouf Basin. Both locations consist of dune terrain and both provide rapid changes in topography of 10s of meters. A second peak of flux was observed over the El Hank region at 23.7°N. Here again, large elevation changes were observed in the surface topography, and the wadis provide a supply of easily erodible material. There is clearly not a one-to-one correspondence between measured wind speeds and measured fluxes. This is to be expected given the altitude at which the measurements are taken and that the emission which led to our flux measurements is dependent upon surface properties as well as wind speed. However all significant fluxes during B600 and B602 occurred in regions where wind speed was above average for the flight. The El Hank region is on the periphery of the jet and it is perhaps surprising to see emission from here, albeit with lower fluxes than to the south. At El Hank the measured wind speeds were < 10 m s^{-1} but to the south were >15 m s^{-1}. This region has a much lower albedo than its surroundings and correspondingly higher surface temperatures which must have decreased stability and increased mixing down of momentum [*Marsham et al.*, 2008; *Huang et al.*, 2010]. The complex terrain will also funnel winds. These factors favor dust emission in this region. This may also mean that at the flight time the mixing of momentum was more advanced and that the winds had passed their peak.

The afternoon B601 flight after LLJ breakdown was much calmer by comparison. The dust concentration was lower and less variable. This flight shows little flux for all regions and the wind speeds had dropped to ~12.5 m s^{-1} at the aircraft altitude. The forecast surface speeds seen in Figure 2 were also much lower. The only small but

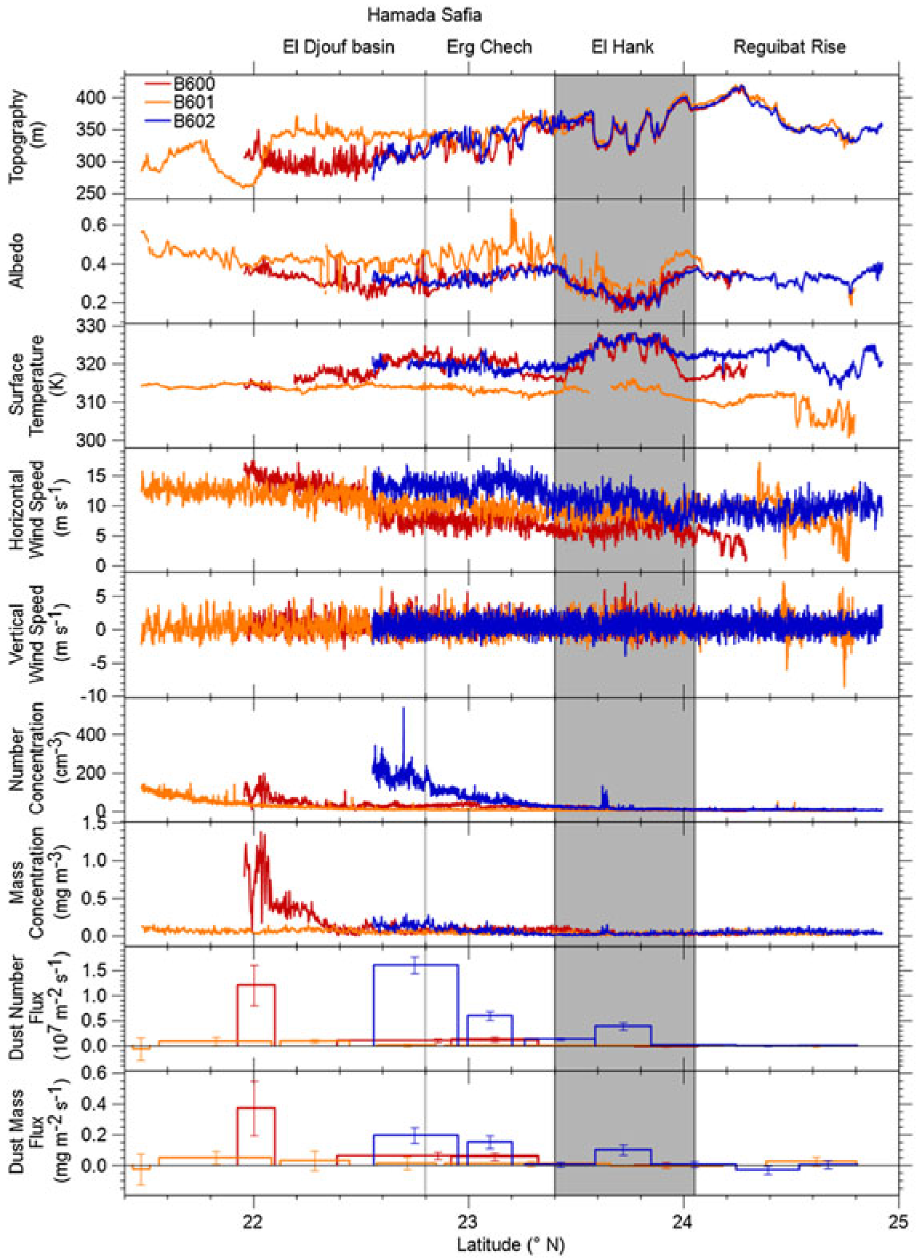

Figure 8. Data collected during long low-level legs of flights B600 and B601 on 17 June 2011 and B602 on 18 June 2011. The minimum altitude was mostly limited to 800–900 m due to low visibility on 17 June 2011; however, between 22.2 and 22.4° during flight B601, the aircraft was able to briefly descend to 500 m altitude. Flight B602 was performed at approximately 100 m altitude. All line charts are 1 s averages, except mass concentration which is a 4 s average to reduce noise. Approximate locations of surface features are labeled above the panels with Hamada Safia and El Hank represented by a gray line and bar, respectively.

significant rise above zero flux was observed at 21.8°N. This coincides with a dry channel which appears to have once drained from a small basin covering ~500 km^2 to the NE. Such a region is likely to contain fluvial deposits available for uplift and also has varying topography. Despite the low flux observed, SEVIRI data in Figure 2 shows the most intense pink dust color at this time. This dust must be previously uplifted, and then mixed up to altitudes where it is more easily identified in SEVIRI imagery.

The peak number fluxes measured during B600 and B602 are of a similar order of magnitude to those of *Sow et al.* [2009], which covered a range of approximately (0.5–5) × 10^7 m^{-2} s^{-1} for two monsoon emission events

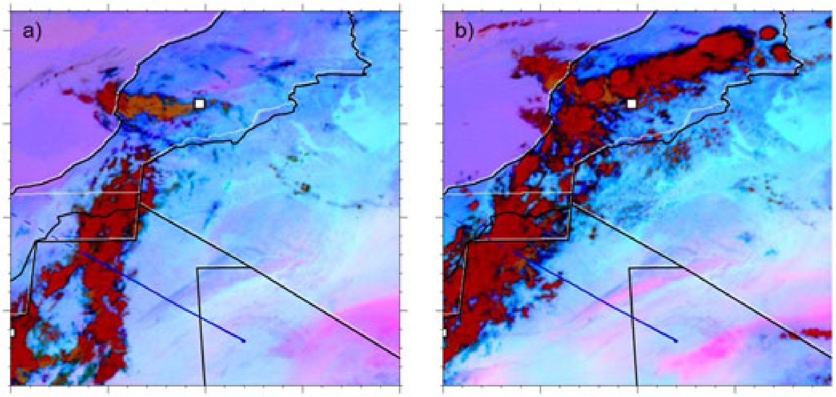

Figure 9. SEVIRI false color image for (a) 0900 UTC and (b) 1400 UTC on the day of flight B602. An increase in pinkness representing local dust uplift or upward vertical mixing of dust can be seen over El Hank and over Erg Chech at the northern edge of the El Djouf basin. The flight track for Flight B602 is overlain as per Figure 1. An animation showing the change is included as supporting information.

and one convective event. We observed peak values of dF_n/dlog(d) of (1–2) × 10^7 m^{-2} s^{-1} for particles with diameters less than 1 μm. This is within the range of approximately (0.6–10) × 10^7 m^{-2} s^{-1} observed in a similar size range by *Sow et al*. [2009]. These values are also similar or slightly higher than those presented by *Gillette et al*. [1972]. The peak mass fluxes are also within the range measured using a TEOM mass balance by *Sow et al*. [2009], giving results which varied from approximately 0.1 to several mg m^{-2} s^{-1}.

During the B600 and B601 flights, there was a large plume of material seen to extend from Algeria over Mali and Mauritania on SEVIRI satellite imagery. It is not immediately clear how much of the dust was transported compared to that which was locally uplifted. However, the largest observed fluxes are clearly linked to this plume. For flight B602, however, there are more local enhancements in dust seen on SEVIRI imagery, allowing us to qualitatively validate the locations of emission by examining the evolution of SEVIRI imagery. Figure 9 shows a comparison of two SEVIRI images from the morning and afternoon of 18 June 2012, before and after the measurements made by flight B602. It is clear that over the intervening time, two isolated pink regions developed in the region over which the measurements were made. The first is a stripe down the approximate center of El Hank and the second is a in a region which follows the Hamada Safia ridge on the northern edge of the El Djouf Basin. These two locations correspond to the two B602 peaks observed in Figure 8 at 22.8 and 23.3°N and this correspondence provides good qualitative support of the results. The SEVIRI detection of dust reaches its peak after the flight because the dust increases in contrast as it accumulates in the boundary layer and as it is mixed upwards.

The ogives presented in Figure 10 show the eddy scales that contributed to the fluxes. For B600 some ogives do not flatten at large wavelengths despite legs of up to 100 km. Such large length scales indicate some contribution of processes other than simple boundary layer turbulence and highlights the difficulty in balancing sufficient counting statistics, covering the lengths scales involved and maintaining homogeneity. The ogives for B602 are well bounded and show contributions from wavelengths of 0.1 to 5 km. This range reflects the fact that the Saharan boundary layer can exceed 5 km in depth. We found that vertical wind spectra follow the Kolmogorov −5/3 power law for eddy length scales between 30 and 400 m. For flight B601 in the late afternoon the length scales are

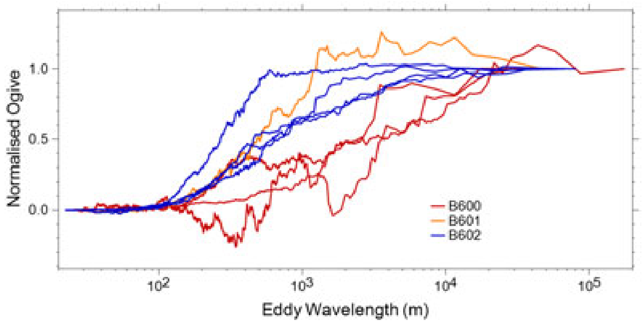

Figure 10. Ogives from flux measurements of the B600, B601, and B602 Harmattan wind cases. Each ogive represents one flux measurement, and the steeper regions of the curves indicate the scales which contribute to the flux. The ogives have been normalized to unity at the largest wavelength. Ogives are only plotted for flux measurements where the uncertainty is less than 100%, i.e., where there is a statistically significant flux.

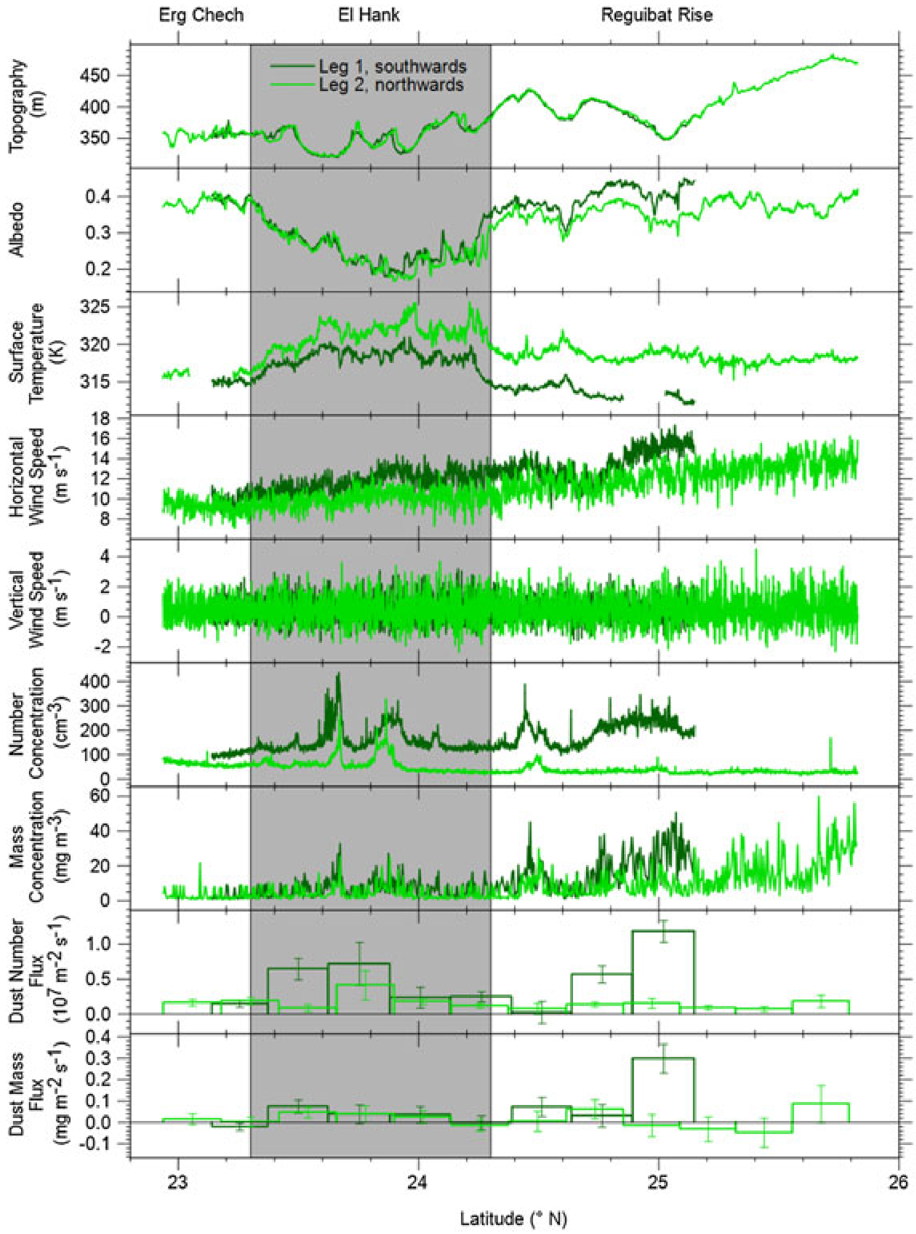

Figure 11. Aircraft measured parameters during the two low-level legs of flight B610 investigating mixing of momentum from a nocturnal low-level jet. All line charts are 1 s averages, except mass concentration which is a 4 s average to reduce noise. Approximate locations of surface features are labeled above the panels with El Hank represented by a gray bar.

similar to those of B602. It is of some note that even for model runs covering large areas of North Africa, grid spacings of below 5 km have been used [*Marsham et al.*, 2011]. When length scales relevant to turbulent fluxes begin to be resolved there are potential issues with related parameterizations. For example gustiness may become resolved which would impact dust uplift schemes, boundary layer eddies would become resolved impacting transport schemes and if similar scales are important for heat and momentum flux then there may be effects related to parameterizations for these properties [e.g., *Wyngaard*, 2004; *Shin and Hong*, 2013].

In all of these cases, the length scales associated with the flux are greater than approximately 0.1 km. Large eddies of this scale are potentially organized features such as rolls or dry convective cells. Such organized structures can include large updraft speeds in the mid boundary layer and will therefore enable efficient mixing of even very large particles through the boundary layer depth. *Shpund et al.* [2011] simulated the impact of large eddies upon sea spray and moisture. They showed that the large eddies cause large particles

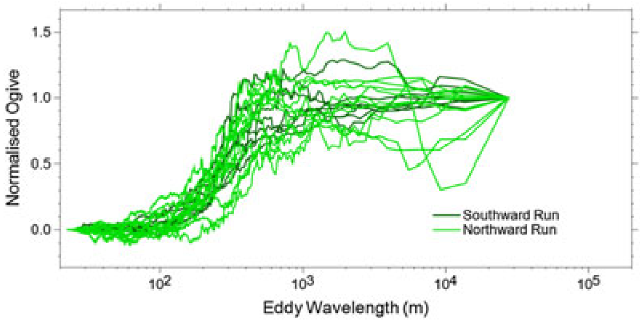

Figure 12. Ogives for each flux measurement of the LLJ flight B610. One ogive has been omitted because the equivalent flux measurement had a very high relative uncertainty. All curves have been normalized to unity at the largest wavelength. The steepest regions indicate the scales which contribute most to the flux.

to be mixed to greater heights in the boundary layer, reduced the gradients of aerosols and droplets and reduced the gradient of the humidity profile. Here we confirm that these large eddy scales dominate the particle flux at the heights measured.

4.3.2. B610 El Hank LLJ

Figure 11 shows measured values for flight B610, analogous to those discussed for flights B600-B602. El Hank is clearly defined by its rugged terrain, its low albedo and a positive surface temperature anomaly of up to 10 K. The dust concentration shows a large amount of variability, with narrow peaks across and just north of El Hank and a broader peak to the north over a valley in Regueibat Rise. As this flight was early in the morning, we expected a shallower convective boundary layer and smaller eddy scales. Each leg is therefore divided into 240 s (~29 km) sections over which the flux was derived. The ogives in Figure 12 show that we have covered all contributing length scales with this integration period and indicate it could be reduced further. Doing so, however, increases the uncertainty in the measurements so gives no real benefit. Two peaks are seen in the fluxes, at latitudes of 23.5°N and on the earlier southward leg at 25°N. The more northerly peak corresponds to the concentration peak above the valley in the Regueibat Rise region where we expect an erodible source of sediments. This peak also corresponds to the highest horizontal wind speeds measured on the legs of 16 m s^{-1}. The small positive surface temperature anomaly in this region may have helped to mix momentum down from the jet. The southern peak was over a valley and ridge of El Hank. Again here we expect to find an ample supply of erodible material, preferential mixing of the LLJ momentum due to the positive surface temperature anomaly and funneling of winds.

On the northward second leg the dust number flux was reduced over El Hank and had dropped to near zero over Regueibat Rise, although the mass flux over El Hank remained at its previous levels. Although there is scope for significant variation within the uncertainty, this indicates a change in the ratio of large and small particle fluxes. The VKE over El Hank was also found to increase between the first and second legs on B610 by between 12 and 34 %. As discussed in 4.1 the change in VKE may be linked to the change in the sizes which contribute to the fluxes. Other possibilities which cannot be verified or discounted by this analysis could include changes in the soil characteristics, perhaps as fine soil was initially eroded exposing coarser soil beneath, or a change in the emission footprint or transport distances of the dust contributing to the flux.

The ogives for the flux measurements are given in Figure 12. They show that for the first leg from approximately 09:14 to 09:45 UTC the important length scales were between 0.1 and 1.0 km. On the reciprocal leg between 09:50 and 10:40 the ogives were more variable and some extended to length scales of 1.2 km. Presumably heterogeneous heating of the surface and boundary layer growth contributed to the variable increase in length scales. Again these scales are typical of large scale organized convection as discussed for the broad Harmattan LLJ case.

4.3.3. B613 Flux Profile

The variation of flux with altitude is expected to be defined by the conditions at the top and bottom of the boundary layer which are a function of dynamics and dust uplift. The surface boundary condition is set by the emission or deposition at this location. The upper boundary is set by the growth rate of the boundary layer and the difference in concentration between the boundary layer and the residual layer or free troposphere above. Between the two boundary conditions we might expect a linear profile of flux with altitude, similar to that observed in other tracers with surface sources such as water vapor [*Stull*, 1988]. This expectation is true of the small particles which dominate the number flux. The flux profile of larger particles may be more complex if they do not follow streamlines.Flight B613 involved multiple legs in the Regueibat

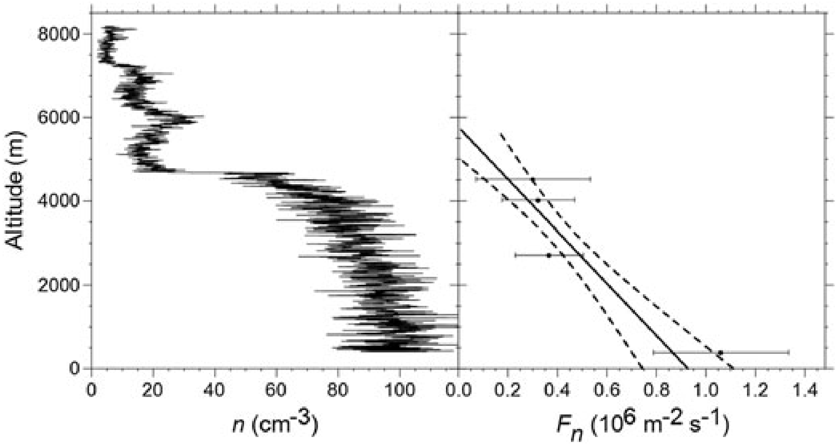

Figure 13. Profile of aerosol number concentration measured during the descent made at the beginning of flight B613 and dust fluxes measured during four legs at different altitudes during the same flight. The solid line is a weighted linear fit and the dashed lines show the fit uncertainties.

region. The flight track incorporated mostly crusted terrain although a depression near the center of the track contained brighter dune material with consequently cooler surface temperatures. Figure 13 shows the number concentration measured on the profile descent through the boundary layer made when the aircraft entered the area of interest and flux measurements derived from horizontal legs subsequently completed moving back up through the boundary layer. The flux profile is consistent with the linear relationship that is expected. All ogives flatten at both ends indicating we have covered all length scales. The boundary layer top can be seen from the number concentration data at 4.5 km. The 0.5 km depth over which the dust concentration decreases is the entrainment zone where clean tropospheric air is being mixed into the boundary layer. In this case the boundary layer is growing slowly in the late afternoon resulting in a near zero flux at the boundary layer top. A moderate flux is observed at 400 m above the surface. Because only a moderate flux was observed the uncertainty for fluxes of particles with diameters greater than 1 μm was generally greater than 100%. For this reason it has not been possible to use the drift velocity analysis to examine the link to the surface. We found that the small particles all have drift velocities much larger than the settling velocity, indicating that the flux is not simply mixing of particles that have undergone long range transport. The negative gradient of the flux profile indicates that the flux cannot be caused by entrainment of clean air at the boundary layer top. Two remaining hypotheses are possible. The first is that the gustiness observed in the wind profile in Figure 3d has generated moderate emission. The second is that the change in wind speed with height seen in Figure 3d has caused advection of dust from different regions at different heights. This could cause a vertical concentration gradient and hence a flux. In this case it is difficult to tell which is the most likely scenario.

Under the assumption that the flux is caused by surface emission, extrapolation of the linear fit across the small distance to the surface results in an estimated surface emission of $(9.3 \pm 1.8) \times 10^5$ m^{-2} s^{-1}. Surface fluxes cannot be derived for other flights as flux profiles were not available.

4.4. Impact of Neglecting Particle Inertia

As discussed previously, particle inertia causes deviation of particles from streamlines and they do not immediately respond to changes in the turbulent wind field. Equation (4) provides a correction factor which may be applied to account for these deviations. The minimum eddy-particle interaction parameter observed is 100, based upon a minimum contributing eddy scale of 0.1 km, the largest velocities of 5 m s^{-1} and the largest relaxation times of 0.2 s for a 300 μm particle. This provides a minimum inertial correction factor very close to 1. The impact of inertia is therefore much lower than other uncertainties and has been neglected.

It is interesting to consider the impact of particles not following streamlines upon the actual flux as well as upon the measurements. Although at the altitude at which the measurements were made we expect even the largest particles measured to follow streamlines, this may not be the case everywhere in the boundary layer or for even bigger particles. Near the surface the eddy scales are smaller and hence streamlines have a higher. These kinds of variations in particle and atmospheric properties cause changes in R and therefore some or all layers of the atmosphere will provide very low turbulent diffusivity for particles above a threshold diameter. Gravitational settling may make these layers impassible. This provides a possible framework for examining how the height at which particles are injected into the atmosphere can affect the maximum size of particles which are mixed through the boundary layer and hence the value of λ derived in this work. The measurements made here are not sufficient to test such a model; modeling of the surface layer may provide some insights. Based upon this framework, however, we expect that the flux of large particles and estimates for λ could only increase for measurements at lower altitudes.

5. Conclusions

The first measurements of size-resolved dust fluxes from an aircraft and the first dust flux measurements from the heart of the Sahara are presented. The benefits of the aircraft platform include an ability to access remote areas, cover multiple regions with different surface properties affecting dust uplift, and the ability to target features of meteorological interest. One particular difficulty is the speed at which the aircraft travels, which impacts its ability to get good counting statistics within a heterogeneous region and measure small-scale turbulence. The other important difficulty is the limit on the lowest altitude at which the measurements can be made, which is dependent upon visibility and affects the ability to link measured fluxes to surface emission without flux profiles being taken. Careful calibration of the instruments and appropriate refractive index corrections of the optical particle counters have ensured that continuous distributions of size-resolved particle fluxes have been possible from ~0.1 to 300 μm diameter, with the upper size only limited by the scarcity of large particles. This size range is more than an order of magnitude larger than has been achieved in previous studies. The methods used have been shown to be robust with ogives indicating that all turbulent scales are captured and with emission locations consistent with SEVIRI satellite observations. Analysis of the size-dependent particle drift velocity and comparison with the particle settling velocity provided validation that measured flux was linked to recent local emission. Positive validation was provided for the three cases closest in time and space to breakdown of a low-level jet. The remaining two cases, including a flux profile, had lower or near zero fluxes, and the number flux of large particles was not great enough to indicate whether the flux in this case was due to local emission. The methods used here are not necessarily limited to dust; particle fluxes of other aerosol types could be measured by the instrument suite on board the FAAM BAe 146 aircraft.

The large measurement range has allowed us to show that the mode in the dust mass flux is at diameters of 30–100 μm, and these large particles provide approximately 90% of the mass flux. This was observed in moderately dusty conditions and in high dust concentrations; i.e., it was a ubiquitous feature of the emission not confined to large events. The largest of these particles would usually be regarded as saltators and not be expected to be lifted above a few cm from the surface. We hypothesize that these particles may be injected to tens or hundreds of meters above the surface by flow separation at ridges, cliffs, or sand dunes. Once at this height, the intense turbulence above the Sahara with typical vertical velocities of ± 4 m s^{-1}, even at 100 m above the surface, is able to suspend these particles and mix them throughout the boundary layer.

The *Kok* [2011a] model of brittle fracture was able to represent the flux size distribution for particles with diameters between 1 and 20 μm. This parameterization predicts a power law distribution with deviations controlled by the geometric mean diameter and standard deviation of the emitting soil, d_s and σ_s, and an empirical scale parameter, λ, which causes drop off at large diameters. The power law distribution in our measurements extended to much larger sizes than suggested by *Kok* [2011a] with values of λ of 43–144 μm compared to the *Kok* [2011a] suggested value of 12 μm. The best fit value of λ correlated well with atmospheric VKE indicating that λ may represent a cutoff controlled by atmospheric turbulent transport rather than the emission process itself. Although this interpretation of λ is due to a completely different mechanism to that suggested by brittle fracture theory, the empirical nature of the scale parameter and scaling function means it is unsurprising that the same functional form fits this data. Another possible explanation for the correlation of λ with VKE would be a correlation of VKE with another atmospheric parameter (e.g., near surface wind speed) which could affect the emission process directly, although such correlations are not well constrained [*Alfaro et al.*, 1997; *Kok*, 2011b]. The scale of turbulence was also shown to affect the flux and measurement of flux when turbulent scales are small and air motion is fast, because large particles are not able to follow the streamlines. It was shown that for the measured conditions the impact was negligible; however, this mechanism may contribute to limiting of the maximum emitted particle diameter in other atmospheric layers. The soil related parameters were required to be much smaller than the values found by *Kok* [2011a] in order to fit our measurements. The surface type affected the flux at small sizes with best fits of d_s and σ_s varying by factors of 2 and 1.5, respectively. The largest values of d_s and σ_s were found over dunes and the smallest over stable terrain. The lack of previous measurement of fluxes of such large particles may be because of the difficulties in measuring such particles with inlet-based instruments or could be because of the hypothesized dependence upon topography which is usually avoided when making flux measurements.

The impact of emission of such large particles will be on local scales due to their high deposition rate. However, they may still affect local radiative transport and cloud processes where they can act as (giant) cloud condensation nuclei. If large particle emission is important in regions outside the Sahara, then the impact will extend to diverse fields such as estimates of air quality in populated areas, aviation hazards from resuspension of volcanic ash, and enhancement of glacier and snow pack melting by albedo reduction.

All the cases presented here were linked to nocturnal low-level jet (LLJ) breakdown phenomena. However, this is a biased sample because LLJs are relatively easy to forecast and target compared to haboobs. Despite the altitude at which the measurements were made, the magnitude of the number and mass fluxes presented here are consistent with or slightly larger than the size-resolved number fluxes measured by *Sow et al.* [2009] and *Gillette et al.* [1972] and the total mass fluxes measured by *Sow et al.* [2009]. We found peak number fluxes, F_n, of $(0.7–1.6) \times 10^7$ m^{-2} s^{-1}, peak mass fluxes, F_m, of 0.20–0.37 mg m^{-2} s^{-1}, and peak values of $dF_n/d\log(d)$ of $(1–2) \times 10^7$ m^{-2} s^{-1}. For each case, the dust flux was found to be highly variable as a function of location. All the highest measurements of dust number flux made during Fennec occurred over regions of varying topography. Although this is consistent with the idea that flow separation is important in lifting particles out of the surface or saltation layer, this work cannot explicitly make a causal link. The correlation may instead be due to the abundance of erodible material at these sites or impacts of the terrain upon local meteorology, such as funneling of winds.

We found that for the relatively simple case where we had emission at the surface and slow growth of the boundary layer into a relatively clean free troposphere, the flux varied linearly with altitude, as expected.

Ogives were used to probe the important length scales over which dust flux occurred. The important length scales for mixing of dust were found to be between 1 and 0.1 km for the earliest measurements of LLJ breakdown at approximately 09:00 UTC. Later in that same flight, around 10:00 UTC, the largest important length scales had increased slightly to approximately 1.2 km and the ogives were more variable. In other flights later in the morning, well-bounded ogives covered scales up to 10 km. Some ogives did not flatten at large scales even out to 50 km, probably indicating mesoscale contamination. By late afternoon, the largest important scales had reduced to 1.4 km. Given that regional research models over the Sahara have been run at 1.5 km, we are entering a "gray zone" where some of this flux is resolved by the model dynamics.

These measurements have prompted a number of hypotheses detailed here. Testing of these hypotheses and assessing of the impact of these findings require further modeling and measurement work. Some particular challenges include testing of how flow separation affects vertical mixing of dust compared to mixing of particles (particularly large particles) from a flat saltation layer and how VKE and the eddy-particle interaction parameter affect subsequent upward transport. The global importance of such processes for large particles is linked to the transport distances of these large particles and assessment of whether emission of such large particles is ubiquitous or occurs only in the Sahara's intense dry convection. These challenges will require the use of regional, global, and large eddy simulations together with observations of transported material [e.g., *Ryder et al.*, 2013a].

Acknowledgments

We would like to acknowledge and thank the following institutions. This work and the Fennec project were funded by the Natural Environment Research Council (NERC) grant NE/G017166/1. Airborne data were obtained using the BAe-146-301 Atmospheric Research Aircraft flown by Directflight Ltd and managed by the Facility for Airborne Atmospheric Measurements, which is a joint entity of NERC and the Met Office. Model simulations were provided by the Met Office. SEVIRI imagery was provided by EUMETSAT and hosted by Imperial College London. Model and airborne data were hosted by the British Atmospheric Data Centre. Surface imagery is courtesy of the Blue Marble Next Generation, Reto Stöckli, NASA Earth Observatory.

We would like to thank Jasper Kok and two other anonymous reviewers for their insightful and valuable contributions.

References

Alfaro, S., A. Gaudichet, L. Gomes, and M. Maillé (1997), Modeling the size distribution of a soil aerosol produced by sandblasting, *J. Geophys. Res.*, *102*(D10), 11,239–11,249, doi:10.1029/97JD00403.

Arnalds, O., F. O. Gisladottir, and H. Sigurjonsson (2001), Sandy deserts of Iceland: An overview, *J. Arid Environ.*, *47*(3), 359–371, doi:10.1006/jare.2000.0680.

Åström, J. A. (2006), Statistical models of brittle fragmentation, *Adv. Phys.*, *55*(3–4), 247–278, doi:10.1080/00018730600731907.

Billesbach, D. P. (2011), Estimating uncertainties in individual eddy covariance flux measurements: A comparison of methods and a proposed new method, *Agric. For. Meteorol.*, *151*(3), 394–405, doi:10.1016/j.agrformet.2010.12.001.

Blackadar, A. (1957), Boundary layer wind maxima and their significance for the growth of nocturnal inversions, *Bull. Am. Meteorol. Soc.*, *38*(5), 283–290.

Blechschmidt, A.-M., J. E. Kristjánsson, H. Ólafsson, J. F. Burkhart, Ø. Hodnebrog, and P. D. Rosenberg (2012), Aircraft-based observations and high-resolution simulations of an Icelandic dust storm, *Atmos. Chem. Phys.*, *12*(22), 10,649–10,666, doi:10.5194/acp-12-10649-2012.

Brindley, H., P. Knippertz, C. Ryder, and I. Ashpole (2012), A critical evaluation of the ability of the Spinning Enhanced Visible and Infrared Imager (SEVIRI) thermal infrared red-green-blue rendering to identify dust events: Theoretical analysis, *J. Geophys. Res.*, *117*, D07201, doi:10.1029/2011JD017326.

Brooks, I., and D. Rogers (2000), Aircraft observations of the mean and turbulent structure of a shallow boundary layer over the Persian Gulf, *Boundary-layer Meteorol.*, *95*(2), 189–210.

Cuesta, J., J. H. Marsham, D. J. Parker, and C. Flamant (2009), Dynamical mechanisms controlling the vertical redistribution of dust and the thermodynamic structure of the West Saharan atmospheric boundary layer during summer, *Atmos. Sci. Lett.*, *10*(1), 34–42, doi:10.1002/asl.207.

Davies, T., M. J. P. Cullen, A. J. Malcolm, M. H. Mawson, A. Staniforth, A. A. White, and N. Wood (2005), A new dynamical core for the Met Office's global and regional modelling of the atmosphere, *Q. J. R. Meteorol. Soc.*, *131*(608), 1759–1782, doi:10.1256/qj.04.101.

Dorsey, J. R., E. Nemitz, M. W. Gallagher, D. Fowler, P. I. Williams, K. N. Bower, and K. M. Beswick (2002), Direct measurements and parameterisation of aerosol flux, concentration and emission velocity above a city, *Atmos. Environ.*, *36*(5), 791–800, doi:10.1016/S1352-2310(01)00526-X.

Drexler, J. M., A. D. Gledhill, K. Shinoda, A. L. Vasiliev, K. M. Reddy, S. Sampath, and N. P. Padture (2011), Jet engine coatings for resisting volcanic ash damage, *Adv. Mater.*, *23*(21), 2419–2424, doi:10.1002/adma.201004783.

Egan, B. A. (1984), Transport and diffusion in complex terrain, *Boundary-Layer Meteorol.*, *30*, 3–28.

Fiedler, S., K. Schepanski, B. Heinold, P. Knippertz, and I. Tegen (2013), Climatology of nocturnal low-level jets over North Africa and implications for modeling mineral dust emission, *J. Geophys. Res. Atmos.*, *118*, 6100–6121, doi:10.1002/jgrd.50394.

Gillette, D. A. (1974), On the production of soil wind erosion having the potential for long range transport, *J. Rech. Atmos.*, *8*, 734–744.

Gillette, D. A., I. H. Blifford Jr., and C. R. Fenster (1972), Measurements of aerosol size distributions and vertical fluxes of aerosols on land subject to wind erosion, *J. Appl. Meteorol.*, *11*, 977–987.

Gillette, D. A., I. H. Blifford, and D. W. Fryrear (1974), The influence of wind velocity on the size distributions of aerosols generated by the wind erosion of soils, *J. Geophys. Res.*, *79*(27), 4068–4075, doi:10.1029/JC079i027p04068.

Heinold, B., P. Knippertz, J. H. Marsham, S. Fiedler, N. S. Dixon, K. Schepanski, B. Laurent, and I. Tegen (2013), The role of deep convection and nocturnal low-level jets for dust emission in summertime West Africa: Estimates from convection-permitting simulations, *J. Geophys. Res. Atmos.*, *118*, 4385–4400, doi:10.1002/jgrd.50402.

Hobby, M., et al. (2013), The Fennec automatic weather station (AWS) network: Monitoring the Saharan climate system, *J. Atmos. Oceanic Technol.*, *30*(4), 709–724, doi:10.1175/JTECH-D-12-00037.1.

Huang, Q., J. H. Marsham, D. J. Parker, W. Tian, and C. M. Grams (2010), Simulations of the effects of surface heat flux anomalies on stratification, convective growth, and vertical transport within the Saharan boundary layer, *J. Geophys. Res.*, *115*, D05201, doi:10.1029/2009JD012689.

Huneeus, N., et al. (2011), Global dust model intercomparison in AeroCom phase I, *Atmos. Chem. Phys.*, *11*(15), 7781–7816, doi:10.5194/acp-11-7781-2011.

Kaufman, Y. J., I. Koren, L. A. Remer, D. Tanré, P. Ginoux, and S. Fan (2005), Dust transport and deposition observed from the Terra-Moderate Resolution Imaging Spectroradiometer (MODIS) spacecraft over the Atlantic Ocean, *J. Geophys. Res.*, *110*, D10S12, doi:10.1029/2003JD004436.

Knippertz, P. (2008), Dust emissions in the West African heat trough—The role of the diurnal cycle and of extratropical disturbances, *Meteorol. Zeitschrift*, *17*(5), 553–563, doi:10.1127/0941-2948/2008/0315.

Kocha, C., P. Tulet, J.-P. Lafore, and C. Flamant (2013), The importance of the diurnal cycle of aerosol optical depth in West Africa, *Geophys. Res. Lett.*, *40*, 785–790, doi:10.1002/grl.50143.

Koehler, K. A., S. M. Kreidenweis, P. J. DeMott, M. D. Petters, A. J. Prenni, and C. M. Carrico (2009), Hygroscopicity and cloud droplet activation of mineral dust aerosol, *Geophys. Res. Lett.*, *36*, L08805, doi:10.1029/2009GL037348.

Kok, J. F. (2011a), A scaling theory for the size distribution of emitted dust aerosols suggests climate models underestimate the size of the global dust cycle, *Proc. Natl. Acad. Sci. U.S.A.*, *108*(3), 1016–1021, doi:10.1073/pnas.1014798108.

Kok, J. F. (2011b), Does the size distribution of mineral dust aerosols depend on the wind speed at emission?, *Atmos. Chem. Phys.*, *11*(19), 10,149–10,156, doi:10.5194/acp-11-10149-2011.

Kok, J. F., E. J. R. Parteli, T. I. Michaels, and D. B. Karam (2012), The physics of wind-blown sand and dust. *Reports Prog. Phys.*, *75*(10), 106901, doi:10.1088/0034-4885/75/10/106901.

Lock, A. P., A. R. Brown, M. R. Bush, G. M. Martin, and R. N. B. Smith (2000), A new boundary layer mixing scheme. Part I: Scheme description and single-column model tests, *Mon. Weather Rev.*, *128*, 3187–3199.

Marsham, J. H., D. J. Parker, C. M. Grams, B. T. Johnson, W. M. F. Grey, and A. N. Ross (2008), Observations of mesoscale and boundary-layer scale circulations affecting dust transport and uplift over the Sahara, *Atmos. Chem. Phys.*, *8*(23), 6979–6993.

Marsham, J., P. Knippertz, N. Dixon, D. J. Parker, and G. M. S. Lister (2011), The importance of the representation of deep convection for modeled dust-generating winds over West Africa during summer, *Geophys. Res. Lett.*, *38*, L16803, doi:10.1029/2011GL048368.

Marsham, J. H., et al. (2013), Meteorology and dust in the central Sahara: Observations from Fennec supersite-1 during the June 2011 Intensive Observation Period, *J. Geophys. Res. Atmos*, *118*, 4069–4089, doi:10.1002/jgrd.50211.

May, P. T. (1995), The Australian nocturnal jet and diurnal variations of boundary-layer winds over Mt. Isa in north-eastern Australia, *Q. J. R. Meteorol. Soc.*, *121*(525), 987–1003, doi:10.1002/qj.49712152503.

McConnell, C. L., E. J. Highwood, H. Coe, P. Formenti, B. Anderson, S. Osborne, S. Nava, K. Desboeufs, G. Chen, and M. A. J. Harrison (2008), Seasonal variations of the physical and optical characteristics of Saharan dust: Results from the Dust Outflow and Deposition to the Ocean (DODO) experiment, *J. Geophys. Res.*, *113*, D14S05, doi:10.1029/2007JD009606.

Netoff, D. I., and M. A. Chan (2009), Aeolian activity at a giant sandstone weathering pit in arid south-central Utah, *Earth Surf. Process. Landforms*, *34*, 99–108, doi:10.1002/esp.1697.

Oerlemans, J., R. H. Giesen, and M. R. Van Den Broeke (2009), Retreating alpine glaciers: Increased melt rates due to accumulation of dust (Vadret da Morteratsch, Switzerland), *J. Glaciol.*, *55*(192), 729–736, doi:10.3189/002214309789470969.

Painter, T. H., A. P. Barrett, C. C. Landry, J. C. Neff, M. P. Cassidy, C. R. Lawrence, K. E. McBride, and G. L. Farmer (2007), Impact of disturbed desert soils on duration of mountain snow cover, *Geophys. Res. Lett.*, *34*, L12502, doi:10.1029/2007GL030284.

Park, S.-U., and E.-H. Lee (2004), Parameterization of Asian dust (Hwangsa) particle-size distributions for use in dust emission models, *Atmos. Environ.*, *38*(14), 2155–2162, doi:10.1016/j.atmosenv.2004.01.024.

Petersen, G. N., and I. A. Renfrew (2009), Aircraft-based observations of air-sea fluxes over Denmark Strait and the Irminger Sea during high wind speed conditions, *Q. J. R. Meteorol. Soc.*, *135*(645), 2030–2045, doi:10.1002/qj.355.

Prata, A. J., and A. Tupper (2009), Aviation hazards from volcanoes: The state of the science, *Nat. Hazards*, *51*(2), 239–244, doi:10.1007/s11069-009-9415-y.

Prospero, J. M., J. E. Bullard, and R. Hodgkins (2012), High-latitude dust over the North Atlantic: Inputs from Icelandic proglacial dust storms, *Science*, *335*(6072), 1078–1082, doi:10.1126/science.1217447.

Reto, S., E. Vermote, N. Saleous, R. Simmon, and D. Herring (2005), The Blue Marble Next Generation—A true color earth dataset including seasonal dynamics from MODIS, NASA Earth Observatory.

Rosenberg, P. D., A. R. Dean, P. I. Williams, J. R. Dorsey, A. Minikin, M. A. Pickering, and A. Petzold (2012), Particle sizing calibration with refractive index correction for light scattering optical particle counters and impacts upon PCASP and CDP data collected during the Fennec campaign, *Atmos. Meas. Tech.*, *5*(5), 1147–1163, doi:10.5194/amt-5-1147-2012.

Ryder, C. L., E. J. Highwood, T. M. Lai, H. Sodemann, and J. H. Marsham (2013a), Impact of atmospheric transport on the evolution of microphysical and optical properties of Saharan dust, *Geophys. Res. Lett.*, *40*, 2433–2438, doi:10.1002/grl.50482.

Ryder, C. L., et al. (2013b), Optical properties of Saharan dust aerosol and contribution from the coarse mode as measured during the Fennec 2011 aircraft campaign, *Atmos. Chem. Phys.*, *13*(1), 303–325, doi:10.5194/acp-13-303-2013.

Schatz, V., and H. J. Herrmann (2006), Flow separation in the lee side of transverse dunes: A numerical investigation, *Geomorphology*, *81*(1–2), 207–216, doi:10.1016/j.geomorph.2006.04.009.

Schepanski, K., I. Tegen, M. C. Todd, B. Heinold, G. Bönisch, B. Laurent, and A. Macke (2009), Meteorological processes forcing Saharan dust emission inferred from MSG-SEVIRI observations of subdaily dust source activation and numerical models, *J. Geophys. Res.*, *114*, D10201, doi:10.1029/2008JD010325.

Schepanski, K., C. Flamant, J.-P. Chaboureau, C. Kocha, J. R. Banks, H. E. Brindley, C. Lavaysse, F. Marnas, J. Pelon, and P. Tulet (2013), Characterization of dust emission from alluvial sources using aircraft observations and high-resolution modeling, *J. Geophys. Res. Atmos.*, *118*, 7237–7259, doi:10.1002/jgrd.50538.

Shao, Y. (2001), A model for mineral dust emission, *J. Geophys. Res.*, *106*(D17), 20,239–20,254, doi:10.1029/2001JD900171.

Shao, Y. (2008), *Physics and Modelling of Wind Erosion*, 2nd ed., Springer, Heidelberg.

Shin, H. H., and S.-Y. Hong (2013), Analysis of resolved and parameterized vertical transports in convective boundary layers at gray-zone resolutions, *J. Atmos. Sci.*, *70*(10), 3248–3261, doi:10.1175/JAS-D-12-0290.1.

Shpund, J., M. Pinsky, and A. Khain (2011), Microphysical structure of the marine boundary layer under strong wind and spray formation as seen from simulations using a 2D explicit microphysical model. Part I: The impact of large eddies, *J. Atmos. Sci.*, *68*(10), 2366–2384, doi:10.1175/2011JAS3652.1.

Sodemann, H., A. S. Palmer, C. Schwierz, M. Schwikowski, and H. Wernli (2006), The transport history of two Saharan dust events archived in an Alpine ice core, *Atmos. Chem. Phys.*, *6*(3), 667–688.

Solomos, S., G. Kallos, E. Mavromatidis, and J. Kushta (2012), Density currents as a desert dust mobilization mechanism, *Atmos. Chem. Phys.*, *12*(22), 11,199–11,211, doi:10.5194/acp-12-11199-2012.

Sow, M., S. Alfaro, J. Rojot, and B. Marticorena (2009), Size resolved dust emission fluxes measured in Niger during 3 dust storms of the AMMA experiment, *Atmos. Chem. Phys.*, *9*(12), 3881–3891.

Stuart, A. (1927), On a black sand from south-east Iceland, *Geol. Mag.*, *64*(12), 540–545, doi:10.1017/S0016756800103899.

Stull, R. B. (1988), *An Introduction to Boundary Layer Meteorology*, Kluwer Acad., Dordrecht.

Sun, D., K. M. Lau, and M. Kafatos (2008), Contrasting the 2007 and 2005 hurricane seasons: Evidence of possible impacts of Saharan dry air and dust on tropical cyclone activity in the Atlantic basin, *Geophys. Res. Lett.*, *35*, L15405, doi:10.1029/2008GL034529.

Tegen, I., and I. Fung (1994), Modeling of mineral dust in the atmosphere: Sources, transport, and optical thickness, *J. Geophys. Res.*, *99*(D11), 22,897–22,914, doi:10.1029/94JD01928.

Todd, M. C., et al. (2013), Meteorological and dust aerosol conditions over the western Saharan region observed at Fennec Supersite-2 during the intensive observation period in June 2011, *J. Geophys. Res. Atmos.*, *118*, 8426–8447, doi:10.1002/jgrd.50470.

Van de Wiel, B. J. H., A. F. Moene, G. J. Steeneveld, P. Baas, F. C. Bosveld, and A. A. M. Holtslag (2010), A conceptual view on inertial oscillations and nocturnal low-level jets, *J. Atmos. Sci.*, *67*(8), 2679–2689, doi:10.1175/2010JAS3289.1.

Washington, R., et al. (2006), Links between topography, wind, deflation, lakes and dust: The case of the Bodélé Depression, Chad, *Geophys. Res. Lett.*, *33*, L09401, doi:10.1029/2006GL025827.

Wyngaard, J. C. (2004), Toward numerical modeling in the "Terra Incognita", *J. Atmos. Sci.*, *61*(14), 1816–1826.

Zhao, C., X. Liu, and L. R. Leung (2012), Impact of the desert dust on the summer monsoon system over southwestern North America, *Atmos. Chem. Phys.*, *12*(8), 3717–3731, doi:10.5194/acp-12-3717-2012.